Cellular water potential sensing via biomolecular condensation

Yunhe Wang[1,2,3], Longchen Zhu[4], Yun Yang[1], Xiaoshuang Li[5], Xin Zhang[4], Xiaofeng Fang[1,2,3*]

[1]Center for Plant Biology, School of Life Sciences, Tsinghua University, Beijing, 100084, China.

[2]Tsinghua University-Peking University Joint Center for Life Sciences, Beijing, China.

[3]State Key Laboratory of Green Biomanufacturing, Beijing, China.

[4]Zhejiang Key Laboratory of Precise Synthesis of Functional Molecules, Department of Chemistry, Westlake University, 600 Dunyu Road, Hangzhou 310030, Zhejiang, P. R. China.

[5]State Key Laboratory of Ecological Safety and Sustainable Development in Arid Lands, Xinjiang Institute of Ecology and Geography, Chinese Academy of Sciences, Urumqi 830011, China

[*]Correspondence: xffang@tsinghua.edu.cn

Abstract

Water molecules, as solvents for biomolecules, are essential to cells. The water potential of the cell decreases under water-deficient conditions[1,2], yet how cells sense changes in water potential remains unknown. Here, we identify a sterile alpha motif (SAM)-containing protein, SAM8, that undergoes water potential-dependent condensation both in vivo and in vitro and is crucial for hyperosmotic stress tolerance and seed germination. We employ biophysical techniques, in vitro reconstitution, and bioimaging to demonstrate that SAM8 is strongly hydrated under normal water conditions, preventing its macroscopic condensation. A negatively charged patch determines SAM8 hydration by creating an electric field and micropolar environment. Water-deficient conditions weaken this hydration, thereby activating SAM8 condensation by reprogramming hydrogen-bond, electrostatic, and hydrophobic interactions. Furthermore, we demonstrate that SAM8 condensates selectively sequester RNA export factors, leading to nuclear retention of mRNAs and translational reprogramming under hyperosmotic stress. Our findings reveal a mechanism by which plant cells directly sense and respond to water status, shedding light on how they adapt to water-deficit conditions.

Main text

Water molecules are central to life, providing a solvent that maintains the functional structures and activities of biomolecules within cells. Cellular water molecules are bound by macromolecules, forming the hydration layer, or freely diffuse in the bulk. These two portions of water are referred to as interfacial water and free water, respectively[1]. Water potential, which can be understood as the availability of free water, governs water uptake from the soil and transport within the plant[3,4]. The cellular water potential is sensitive to environmental

fluctuations, particularly drought, high salinity, and temperature stress[1,2,5]. Biomolecules in living cells are surrounded by at least a molecular layer of hydrated water[6]. Cellular water potential reduction decreases hydration of biomolecules, compromising membrane integrity, disrupting the three-dimensional structures of proteins and impairing enzymatic activities, etc[7]. Therefore, cellular water potential sensing and response are crucial for plant development and adaptation to different environmental stresses, the mechanism of which, however, remains unknown.

SAM8 undergoes cellular water potential-dependent condensation in cells

Biomolecular condensation is emerging as a key mechanism for sensing and responding to environmental stress[8,9]. Hyperosmotic stress often induces cell volume shrinkage, resulting in membrane tension changes, water potential reduction and subsequent dehydration of biomolecules, increased molecular crowding and ion concentration[10] (Fig. 1a, Extended Data Fig. 1a). Both nuclear and cytoplasmic proteins were reported to sense hyperosmotic stress via molecular crowding-dependent condensation in plants[11,12]. We reasoned that biomolecular condensation can be a way of sensing cellular water potential changes because hydration of biomolecules tunes the strength of hydrophobic interactions, electrostatic interactions, or the cation–π interactions, all of which are the driving force for condensation. Deuterium oxide (D_2O) forms stronger hydrogen bonds than H_2O, strengthening water-water interactions while reducing water-protein interactions[13-17]. Therefore, we used D_2O treatment to reduce the hydration of proteins without affecting cell volume (Fig. 1a and Extended Data Fig. 1b).

To understand how plant cells directly sense water potential, we searched for D_2O-dependent condensation by expressing proteins with the potential to undergo phase separation[18] in cells and challenged the cells with isosmotic buffer prepared with D_2O. From this screen, we discovered a few proteins that formed condensates in tobacco cells in response to D_2O treatment (Supplementary Table 1). Among them, At5g23680, which encodes a sterile alpha motif (SAM) domain-containing protein named SAM8, formed nuclear condensates in tobacco and yeast cells upon D_2O treatment (Fig. 1b, c). We next generated SAM8 complementation lines (*SAM8pro::SAM8-mVenus*) in *sam8-1* knockout plants (Extended Data Fig. 3b-d). In root tip cells, SAM8-mVenus was diffuse in the nucleoplasm but formed nuclear condensates when plants were transferred into isosmotic buffer containing more than 40% D_2O for 5 minutes (Fig. 1d, Extended Data Fig. 1c, d; Supplementary Video 1). D_2O-induced condensation of SAM8 was confirmed by immunostaining (Extended Data Fig. 1e). As a comparison, two known phase-separating proteins SEUSS and DCP5[11,12], did not form condensates upon D_2O treatment (Extended Data Fig. 1f). These observations indicate that the response of SAM8 to D_2O is

genuine and specific.

We next tested whether SAM8 condensation is responsive to water potential change induced by hyperosmotic stress. SAM8 rapidly formed condensates in tobacco epidermal cells (Extended Data Fig. 1g), yeast cells (Extended Data Fig. 1h), and Arabidopsis root tip cells (Fig. 1e) when cells were treated with hyperosmotic stress. The threshold of water potential change for SAM8 condensation was approximately 0.3-0.35 MPa (Extended Data Fig. 1i, j). The condensates are highly dynamic as they dissolved within 20 min upon stress removal (Fig. 1e), and exhibited fast recovery of fluorescence after photobleaching (Extended Data Fig. 1k). Ethylene glycol (EG), which does not cause molecular crowding but reduces cellular water potential[12], triggered SAM8 condensation (Fig. 1f), indicating that SAM8 condensation is not dependent on molecular crowding. Treatment with abscisic acid (ABA) and reactive oxygen species (H_2O_2), both of which are early signals in osmotic signaling, did not induce SAM8 condensation (Extended Data Fig. 1l). In addition, chemical inhibition of calcium influx by $LaCl_3$ or genetic ablation of Raf-like kinases (*ok130-null mutant*)[19] had neglectable impact on SAM8 condensation (Extended Data Fig. 1m, n). These results indicate that SAM8 condensation is independent of known osmotic signaling pathways.

The processes of seed ripening and germination experience significant changes in cellular water potential (Fig. 1g). SAM8 is highly expressed in seed and root tissues (Extended Data Fig. 3a), prompting us to examine SAM8 condensation during seed development and germination. In the course of seed development, when the embryos are still wet, SAM8 was diffused within the nucleus (Fig. 1h). Concomitant with dehydration during the late stages of seed development and in dry seeds, SAM8 formed condensates (Fig. 1h, i). Upon imbibition in water but not NaCl solution, SAM8 condensates rapidly dissolved within 10-20 min (Fig. 1i). When water-imbibed seeds were transferred into NaCl solution, SAM8 condensates reappeared (Fig. 1i), suggesting that SAM8 condensation dynamically responds to water potential changes in seeds.

Temperature also tunes cellular water potential[5,20]. It has been reported that temperature increases and decreases antagonize and synergize with hyperosmotic treatments, respectively, in terms of cellular water potential[1]. Indeed, we found that hyperosmotic treatment at 35°C induced fewer SAM8 condensates than at 25°C, whereas treatment at 15°C markedly enhanced its condensation in yeast cells (Extended Data Fig. 1o, p). Statistical analysis revealed a significant interaction between external osmotic strength and temperature for SAM8 condensation (Extended Data Fig. 1p), indicating that temperature and osmotic stress jointly regulate SAM8 condensation. Similarly, in Arabidopsis roots, while hyperosmotic treatment at 25°C triggered SAM8 condensation within 5 minutes, the same osmotic strength at 37°C failed to

induce SAM8 condensation even within 20 minutes (Extended Data Fig. 4a). Taken together, these data indicate that SAM8 undergoes water potential-dependent condensation in cells.

IDR2 and the SAM domain are both necessary for SAM8 condensation

SAM8 contains a sterile alpha motif (SAM) domain at its C terminus[21] (Fig. 2a, Extended Data Fig. 2a). The remaining regions were largely unfolded (Extended Data Fig. 2a) and predicted as intrinsically disordered regions (IDRs, Fig. 2a). The SAM domain is a classic oligomerization domain that undergoes head-to-tail assembly and was reported to mediate phase separation[22,23]. Sequence-based predictions indicated that three positively charged amino acids (280R, 281R, 282K) in the end helix surface are important for SAM8 oligomerization (Fig. 2a, Extended Data Fig. 2b). Indeed, *in vitro* purified SAM domain mainly existed as oligomers, but substituting the three RRK residues with negatively charged glutamic acid residues (SAM^{RRKm}) converted SAM to monomer (Fig. 2b). To investigate the contribution of each region to SAM8 condensation, we generated truncation or mutation variants and tested their condensation in tobacco cells. Deletion of IDR1 resulted in partial cytoplasmic distribution of SAM8 but retained osmotic-dependent condensation, whereas deletion of IDR2 abolished SAM8 condensation (Fig. 2c). SAM8 with the SAM domain deleted ($SAM8^{\Delta SAM}$) or mutated ($SAM8^{RRKm}$) failed to form condensates (Fig. 2c). In line with this, co-expression of $SAM8^{\Delta IDR2}$ and $SAM8^{RRKm}$ is sufficient to reconstitute osmotic-dependent condensation (Extended Data Fig. 2c). The necessity of IDR2 and SAM domain in SAM8 condensation was further confirmed in yeast cells (Extended Data Fig. 2d). In *Arabidopsis* stable transgenic plants, $SAM8^{\Delta IDR2}$ and $SAM8^{RRKm}$ failed to form condensates upon mannitol (Fig. 2d) or D_2O (Extended Data Fig. 2e) treatment. These results indicate that both IDR-mediated interactions and SAM-mediated oligomerization are required for SAM8 condensation.

SAM8 condensation is critical for osmotic tolerance and seed germination

We next assessed the functional significance of SAM8 condensation. We obtained two mutant alleles: *sam8-1* contains a T-DNA insertion that abolishes SAM8 expression (Extended Data Fig. 3b-d); *sam8-2* is a CRISPR mutant with a 1-bp insertion that causes a premature stop codon (Extended Data Fig. 3b). Under normal growth conditions, *sam8* mutants were phenotypically indistinguishable from wild-type Col-0 (Fig. 2f, g). When plants were exposed to hyperosmotic stress, while cell growth in the root apical meristem and root extension rate were inhibited in Col-0 during the first few days and partially recovered (Fig. 2e, f; Extended Data Fig. 3e-h), suggesting an adaptive strategy that balances growth with stress tolerance, this inhibition and recovery were significantly compromised in *sam8* mutants (Fig. 2 e, f; Extended Data Fig. 3e-h). This led to the hypothesis that impaired growth inhibition under osmotic stress increases stress sensitivity and possibly cell death. Indeed, SYTOX

Green staining revealed substantially higher cell death rates in the *sam8-1* and *sam8-2* mutants than in Col-0 (Extended Data Fig. 3i, j), and the survival of *sam8-1* and *sam8-2* seedlings under hyperosmotic stress was significantly reduced (Fig. 2g, h). The hypersensitivity of the *sam8-1* mutant can be fully rescued by wild-type SAM8 but not by the condensation-defective variants (Fig. 2i, j). These data indicate that SAM8 condensation is essential for osmotic stress adaptation and tolerance.

In nature, hyperosmotic stress frequently coincides with higher ambient temperature or heat stress[24]. The dependence of SAM8 condensation on both osmotic potential and temperature (Extended Data Fig. 4a) prompted us to test whether SAM8 condensation mediates the combined effects. Indeed, we found that hyperosmotic treatment at higher ambient temperature (26°C) dramatically increased death rates of wild-type plants compared to the same osmotic strength at 22°C (Extended Data Fig. 4b-e). The *sam8-1* mutant plants invariably displayed minimal root growth upon osmotic treatment at both temperatures (Extended Data Fig. 4c-e). Consistent with this, when germinated and grown on hyperosmotic stress medium at two different temperatures, the majority of Col-0 seedlings survived at 22°C, but approximately 35% of them died at 26°C (Extended Data Fig. 4f, g). The *sam8* mutant plants were similarly sensitive to osmotic stress at 22°C and 26°C, and SAM8-complemented plants behaved like Col-0 (Extended Data Fig. 4f, g). In contrast, overexpression of SAM8 increased the propensity for condensation (Extended Data Fig. 4h) and enhanced plant survival at both 22°C and 26°C (Extended Data Fig. 4f, g). SAM8 thus represents one of the intracellular modules for integrating osmotic stress and temperature via water-potential-dependent condensation.

Given that SAM8 condensation also responds to water potential changes in seeds (Fig. 1h, i), we explored the function of SAM8 in seed germination. The results showed that both *sam8-1* and *sam8-2* exhibited delayed germination rate compared to Col-0 (Extended Data Fig. 4i). This defect was fully rescued by wild-type SAM8 but not by condensation-defective variants (Extended Data Fig. 4j). Taken together, these data indicate that water potential-dependent condensation of SAM8 is required for osmotic tolerance and plays a role in seed germination.

SAM8 phase separation in vitro is sensitive to water potential change

To provide a mechanistic understanding of water potential-dependent condensation, we purified SAM8 (Extended Data Fig. 5a, b) and assessed the phase behavior in vitro. SAM8-GFP protein was homogenously diffused but formed sphere droplets upon addition of PEG8000 (Fig. 3a, Extended Data Fig. 5c). However, addition of dextran or ficoll, which are widely used as model crowders in phase separation assays[25], failed to trigger SAM8 phase separation (Fig. 3a). We confirmed this using a previously described crowding

sensor, IDR1 of SEU[11], finding that although 4% PEG and 7.5% dextran similarly induced IDR1^{SEU} phase separation, 4% PEG but not 7.5% dextran induced SAM8 phase separation (Extended Data Fig. 5c).

Although PEG and dextran are similar in their ability to induce crowding, PEG can constrain many more water molecules than dextran and thus greatly lowers the water potential[1,26]. We verified this by vapour-pressure osmometry measurements (Fig. 3b). The hyper-sensitivity of SAM8 to PEG but not dextran suggests that SAM8 phase separation in vitro is water potential-dependent. Consistently, SAM8-GFP formed condensates in D_2O- but not H_2O-prepared buffer (Extended Data Fig. 5d), and the small molecule 2,2,2-Trifluoroethanol (TFE), which has a strong ability to displace the hydrating water molecules from biomolecules[27], induced the condensation of SAM8 (Extended Data Fig. 5e).

SAM8 condensation was not affected by GFP tag, as untagged SAM8 also formed condensates upon addition of D_2O or PEG (Extended Data Fig. 5d, f). As a control, the condensation of SEUSS-IDR1[11], DCP5-ICS[12], and FREE1[28], was unaffected by D_2O (Extended Data Fig. 5d). Consistent with in vivo observations, the ability of SAM8 to phase separate in vitro was largely dependent on IDR2 and the SAM domain (Extended Data Fig. 5g, h). These data indicate that SAM8 condensation is intrinsically sensitive to reductions in water potential.

SAM8 has a thick hydration layer

To understand the molecular basis of water potential response, we interrogated the hydration of SAM8. We used dynamic light scattering[29] and multi-angle light scattering[30] to measure the hydration radius (Rh) and actual size (or radius of gyration, Rg) of SAM8, respectively (Fig. 3c). We found that Rh of SAM8 was significantly bigger than Rg (Fig. 3d), consistent with an unusually hydrated state and/or expanded conformation. As a control, there is no obvious difference between the Rh and Rg of SOSEKI1[31] and SAM7[21] (Extended Data Fig. 5i), both of which contain polymerization domains. In line with the ability of PEG to compete for hydration, the Rh of SAM8 was decreased by PEG addition (Fig. 3e). PEG has less impact on water potential at higher temperature[1] (Extended Data Fig. 5j, k). We found that the size of SAM8 droplets decreased significantly at 37°C compared to that at 25°C in the presence of the same amount of PEG (Extended Data Fig. 5l, m). By comparison, the droplets of IDR1^{SEU} showed no noticeable change at two temperatures (Extended Data Fig. 5l, m). Taken together, these results demonstrate that SAM8 possesses a thick hydration shell and that a reduction in water potential leads to its phase separation in vitro.

The molecular basis of water potential sensing by SAM8

We next explored the mechanism underlying SAM8 hydration. Analysis of net

charge showed that the IDR3 of SAM8 is highly negatively charged (Fig. 3f, Extended Data Fig. 6a). Energy calculations using the AMOEBA force field showed that Asp and Glu have very low intrinsic free energies of hydration[32]. We therefore hypothesized that the negative charges within IDR3 are the main determinant for SAM8 hydration. To test this, we generated a SAM8 variant ($SAM8^{IDR3mQ}$) by mutating Asp and Glu within IDR3 into Asn and Gln, respectively (Fig. 3f). Distinct from wild-type SAM8, $SAM8^{IDR3mQ}$ showed no difference in its Rh and Rg (Fig. 3g) and formed condensates without the need for PEG (Fig. 3h). To decouple the contribution of electrostatic repulsion and hydration in SAM8 condensation, we mutated 10 core aspartate/glutamate residues within IDR3 into serine ($SAM8^{IDR3mS}$, Extended Data Fig. 6b, c) to preserve hydration but not electrostatic interactions, as serine is polar and attracts water molecules via dipole-dipole interactions. We also generated $SAM8^{IDR3mK}$ and $SAM8^{IDR3mR}$ (Extended Data Fig. 6b, c) to preserve electrostatic repulsion and disrupt hydration, as lysine and arginine are less potent at hydration than aspartate and glutamate[32]. Biophysical analyses confirmed that the Rh and Rg of $SAM8^{IDR3mS}$ showed a significant difference, whereas those of $SAM8^{IDR3mK}$ and $SAM8^{IDR3mR}$ displayed less or no difference (Extended Data Fig. 6d). Consistently, $SAM8^{IDR3mS}$ formed condensates in a PEG-dependent manner, whereas $SAM8^{IDR3mK}$ and $SAM8^{IDR3mR}$ formed constitutive condensates without PEG (Extended Data Fig. 6e). These results indicate that the negatively-charged IDR3 controls SAM8 condensation primarily via its potent hydration.

Next, we performed FLIM-FRET assays to examine the intermolecular interactions of SAM8 under changing water potentials (Fig. 3i). $SAM8^{\Delta SAM}$ was used to avoid the dominant impact of SAM oligomerization on FRET signal. The results revealed gradual enhancement of SAM8 intermolecular interactions upon increasing the concentration of PEG (Fig. 3j), NaCl (Extended Data Fig. 6f, g), mannitol (Extended Data Fig. 6h, i), but not Dextran (Fig. 3k). It is noteworthy that the water potential threshold for SAM8 interactions in vitro (Fig. 3b) is similar to that of SAM8 condensation in vivo (Extended Data Fig. 1i, j), suggesting that SAM8 senses water potential thresholds of physiological relevance. Disruption of the negative charges within IDR3 significantly enhanced the intermolecular interactions (Fig. 3l). Collectively, these data demonstrate that reduced water potential directly promotes SAM8 self-interaction and triggers condensate formation.

Given the strong charge-dipole interactions and hydrogen-bonding capacity of negatively charged amino acids, we next tested whether the negative charges set up an electric field around SAM8, which could polarize and constrain water molecules[33]. To this end, we probed the microenvironment of SAM8 condensates. The Di-4-ANEPPS can be used to measure local electric field[34,35]. We found that SAM8 condensates exhibited a significantly higher ANEPPS

signal ratio than condensates of SAM8^{IDR3mQ} (Fig. 3m, n) and other mutant variants (Extended Data Fig. 6j, k), indicating a stronger electric field within SAM8 condensates. The SBD-related fluorophore has been used to measure the micropolarity of condensates as its fluorescence lifetime decreases with increasing micropolarity[36]. SAM8 condensates exhibited shorter fluorescence lifetime than SAM8^{IDR3mQ} condensates (Fig. 3o, p). Together, these results indicate that negative charges within IDR3 endow SAM8 hydration, preventing its condensation under water-rich conditions.

Conservation analysis of SAM8 condensation

We performed a phylogenetic analysis and identified SAM8 homologs in all land plants (Extended Data Fig. 7a). These SAM8 homologs contain a highly conserved C-terminal SAM domain, juxtaposed by a conserved negative patch (Extended Data Fig. 7a). Notably, the degree of negative charge varies among SAM8 homologs, prompting us to test if this correlates with the threshold of water potential for condensation. We found that SAM8 from *Camelina sativa (Cs)*, which is a drought-tolerant crop that can be grown in environment with limited water availability[37], showed high sequence homology with Arabidopsis SAM8 but contains longer stretch of negatively charged amino acids in IDR3 region (Extended Data Fig. 7b). In vitro, *Cs*SAM8 required slightly higher PEG8000 concentrations to induce its phase separation compared to *At*SAM8 (Extended Data Fig. 7c). When expressed in yeast cells, both *At*SAM8 and *Cs*SAM8 formed more condensates upon increasing sorbitol concentration, supporting the conservation of SAM8 response to water potential. However, *Cs*SAM8 formed fewer condensates than *At*SAM8 upon the same sorbitol treatment (Extended Data Fig. 7d), suggesting that *Cs*SAM8 has more negative water potential threshold. We then generated complementation Arabidopsis plants expressing *Cs*SAM8 under the *At*SAM8 promoter in the *sam8-1* mutant background. Compared to *At*SAM8, a smaller number of condensates were observed for *Cs*SAM8 upon treatment by the identical concentration of mannitol or percentage of D_2O (Extended Data Fig. 7e). In the root extension assay, we found that *CsSAM8/sam8-1* plants were less inhibited by the same osmotic stress than *AtSAM8/sam8-1* plants (Extended Data Fig. 7f-i). In line with this observation, SAM8^{IDR3mQ} constitutively formed nuclear condensates in root tip cells under normal growth condition (Fig. 3q), and *SAM8^{IDR3mQ}/sam8-1* plants displayed retarded growth and development compared to wild type or *SAM8/sam8-1* plants (Extended Data Fig. 7j). Together, these results indicate that the ability to sense water potential change by SAM8 is conserve and crucial for balancing growth and osmotic tolerance.

SAM8 condensates selectively partition RNA export factors

Nuclear mRNA export is an essential RNA surveillance step for proper gene expression[38,39]. Recent structural analysis of human mRNA export complex revealed that ALYREF (ALY) recognizes mRNA ribonucleoprotein complexes

(mRNPs) via exon junction complex (EJC) and connects it with transcription–export complex (TREX) through UAP56, forming TREX-mRNP complexes that are competent for subsequent export (Fig. 4a)[40,41]. To elucidate the molecular function of SAM8 condensation, we searched for SAM8-interacting proteins via immunoprecipitation under hyperosmotic stress. Gene Ontology analysis revealed significant enrichment for components involved in the mRNA surveillance pathway and RNA splicing (Extended Data Fig. 8b). Notably, several RNA export factors were identified in the interactome, including all four members of the ALY family[42] and EJC subunit EIF4A3[43] (Extended Data Fig. 8a; Supplementary Table 2). The interactions between SAM8 and ALYs and EIF4A3 were validated by co-immunoprecipitation (Fig. 4b), bimolecular fluorescence complementation (Extended Data Fig. 8c), and FLIM-FRET (Extended Data Fig. 8d) assays. In tobacco epidermal cells, ALYs and EIF4A3 were diffused in the nucleolus and nucleoplasm, consistent with their localization in Arabidopsis[42,43] (Fig. 4c). Upon hyperosmotic treatment, ALYs and EIF4A3 were highly enriched in SAM8 condensates (Fig. 4c), suggesting that SAM8 condensates partition ALYs and EIF4A3. Similarly, ALYs and EIF4A3 were recruited by SAM8 droplets in vitro (Fig. 4d).

The ALY family proteins possess a conserved central RRM domain and nonspecifically bind single-stranded RNAs[42]. We found that ALY1 formed droplets together with a 35-nucleotide PolyA RNA (Extended Data Fig. 8e). Intriguingly, when ALYs/RNA was incubated with SAM8, ALYs/RNA droplets formed subphases within SAM8 droplets (Extended Data Fig. 8f), reminiscent of coexisting multiphases formed by nucleolar proteins[44]. The ALY-RNA subphase formation occurs irrespective of the order of component addition or incubation duration (Extended Data Fig. 8g, h). This is likely due to the higher micropolarity of SAM8 condensates or the different strength of interactions between SAM8, ALYs, and RNA. Nevertheless, these observations further support that SAM8 condensates partition ALYs/RNA complexes.

Arabidopsis ALYs interact directly with UAP56[42]. Consistently, UAP56 was recruited into ALY1 droplets in vitro (Fig. 4e). However, UAP56 was not found in SAM8 immunoprecipitation (Supplementary Table 1) and was not recruited by SAM8 condensates both in vitro and in tobacco cells (Extended Data Fig. 8i). When increasing concentrations of SAM8 were added to ALY1/UAP56, ALY1 but not UAP56B was partitioned into SAM8 droplets (Fig. 4e, f). Co-expression in tobacco cells confirmed that SAM8 condensates recruit ALY1 and EIF4A3 and exclude UAP56 (Fig. 4g). These findings suggest that SAM8 condensates can disrupt the association between ALY and UAP56 via selective partitioning.

SAM8 condensation inhibits mRNA export and reprograms the translatome

The selective recruitment of RNA export factors by SAM8 condensates prompted us to hypothesize that SAM8 condensation inhibits mRNA transport. To test this, we detected mRNA localization by fluorescence in situ hybridization (FISH) with oligo(dT) probes. In wild-type Col-0, the mRNA signal was distributed evenly in the nucleus and cytoplasm under normal growth conditions (Fig. 5a, b), but showed a significantly higher nuclear-to-cytoplasmic ratio upon osmotic treatment (Fig. 5a, b). In contrast, the *sam8-1* mutant displayed a similar nuclear-to-cytoplasmic mRNA ratio under normal and osmotic stress conditions (Fig. 5a, b). These findings indicate that osmotic stress elicits nuclear retention of mRNA in a SAM8 condensation-dependent manner.

To test how this retention regulates translation, we calculated the global translation efficiency (TE) via parallel mRNA-seq and Ribo-seq in Col-0, *sam8-1,* and *sam8-2* under normal conditions and upon hyperosmotic treatment (see Extended Data Fig. 9a, b for quality control). The results revealed substantial differences in hyperosmotic-induced translation efficiency (TE) changes in Col-0 (Fig. 5c). Gene Ontology (GO) analysis showed that TE-upregulated genes were enriched in responses to various stresses, whereas TE-downregulated genes were enriched in growth and development (Extended Data Fig. 9c), indicating that plants balance growth and stress defense via reprogramming translation. In contrast, TE changes induced by hyperosmotic treatment were much smaller in *sam8* mutants (Fig. 5d, Extended Data Fig. 9d) and showed less than 1% of overlap with those of wild-type (Fig. 5e), supporting that SAM8 is important for the translation reprogramming in response to osmotic stress. Comparison of translational efficiency between *sam8-1* and wild-type showed marked changes under both mock and osmotic stress conditions (Extended Data Fig. 9e, f). GO analysis showed that these TE-changed genes were mainly enriched in development- and stress-related processes (Fig. 5f and Extended Data Fig. 9g), indicating a role of SAM8 in balancing growth and stress defense. To confirm the translation of candidate transcripts, we performed a polysome profiling assay (Extended Data Fig. 9h). Translational efficiency was calculated as the ratio of RNA levels in polysomal fractions to total transcripts by quantitative RT-PCR. Consistent with the Ribo-seq results, the translation of *ABF4* (*ABRE BINDING FACTOR 4*) and *DREB2A* (*DEHYDRATION-RESPONSIVE ELEMENT-BINDING PROTEIN 2*), which encode important osmotic stress regulators, were upregulated by osmotic stress in Col-0 but not in *sam8-1* mutant (Fig. 5g). Translation of transcripts encoding key regulators of root meristem cell growth, such as *LHW* (*LONESOME HIGHWAY*) and *RGI4* (*RGF1 INSENSITIVE 4*), were significantly downregulated by osmotic stress in Col-0 but remained largely unchanged in *sam8-1* mutant (Fig. 5g). As a control, the translational efficiency of *UBC10* was unaffected (Fig. 5g). Taken together, these results indicate that SAM8 condensation under osmotic stress promotes stress-adaptive translation and suppresses growth-related translation via regulating mRNA export.

If nuclear retention of mRNAs under osmotic stress is important for osmotic stress adaptation, boosting mRNA nuclear export should be disadvantageous to osmotic tolerance. Indeed, we found that overexpression of ALYs as well as EIF4A3 in wild-type Col-0 background led to hypersensitivity to osmotic stress than the wild type (Fig. 5h, i; Extended Data Fig. 10a-c). These data indicate that SAM8 condensation-dependent regulation of RNA export finetunes the balance between growth and defense and promotes osmotic tolerance.

Discussion

Our results collectively support that SAM8 is a direct cellular water potential sensor. SAM8 possesses SAM-mediated oligomerization and IDR-mediated weak multivalent interactions, making it prone to condensation. However, a negatively charged region within SAM8 establishes an electric field that enables thick hydration. As such, under conditions in which cellular water is abundant, SAM8 hydration prevents its condensation. Once water potential is reduced under water-scavenging conditions such as drought or high salinity, hydration is reduced, activating SAM8 condensation (Fig. 5j). SAM8 condensates selectively include and exclude RNA export factors, leading to mRNA retention and translational reprogramming (Fig. 5j).

While biomolecular condensate formation is generally affected by water–protein interactions[45], protein–protein interactions also contribute substantially to the thermodynamic driving forces of biomolecular condensation[46]. SAM8 is unique in that it has both strong protein–protein interactions that are mediated by the SAM domain and protein–water interactions enabled by the negatively charged patch. We believe that the combination and balance between protein–protein and protein–water interactions are crucial for water potential sensing. Many other polymerization domains and hydrophobic regions are involved in biomolecular condensation[16,23]. Our findings shed light on the discovery or engineering of different water potential sensors.

In response to diverse stresses, eukaryotic cells activate the integrated stress response (ISR), the core of which is to attenuate global protein synthesis while promoting the selective translation of specific mRNAs[47]. Indeed, translation of many mRNAs was inhibited under hyperosmotic stress in plants[12]. RNA export is an important process to ensure the continuity between transcription and translation[48]. Our results indicate that SAM8 condensation reprograms translation via controlling mRNA export, representing one of the strategies to adjust translation under hyperosmotic stress in plants. Zander et al. reported that RNA export acts as a surveillance mechanism under heat stress in *Saccharomyces cerevisiae*[49]. Heat induces the dissociation of RNA export factor Mex67 from regular mRNAs to prevent general mRNA export. In contrast, heat-shock mRNAs are rapidly exported and preferentially translated,

facilitating cell survival under extreme situations[49]. It is well-established that the balance between stress resistance and growth is finely tuned[50]. SAM8 condensation could be a mechanism for maintaining such balance. Our next step is to test whether certain stress-related mRNAs can evade SAM8-dependent retention and be selectively exported to the cytoplasm in plants.

References

1 Watson, J. L. *et al.* Macromolecular condensation buffers intracellular water potential. *Nature* **623**, 842–852 (2023).

2 Xiong, L. & Zhu, J. K. Molecular and genetic aspects of plant responses to osmotic stress. *Plant Cell Environ* **25**, 131–139 (2002).

3 Slatyer, R. Plant-water relationships. *London and New York: Academic Press* (1967).

4 De Swaef, T. *et al.* On the pivotal role of water potential to model plant physiological processes. *in silico Plants* **4**, 1–28 (2022).

5 Lau, E. Y. & Krishnan, V. V. Temperature dependence of protein-hydration hydrodynamics by molecular dynamics simulations. *Biophys Chem* **130**, 55–64 (2007).

6 Lang, X., Shi, L., Zhao, Z. & Min, W. Probing the structure of water in individual living cells. *Nat Commun* **15**, 5271 (2024).

7 Zhao, C., Zhang, H., Song, C., Zhu, J. K. & Shabala, S. Mechanisms of Plant Responses and Adaptation to Soil Salinity. *Innovation (Camb)* **1**, 100017 (2020).

8 Alberti, S. & Hyman, A. A. Biomolecular condensates at the nexus of cellular stress, protein aggregation disease and ageing. *Nat Rev Mol Cell Biol* **22**, 196–213 (2021).

9 Peng, J., Yu, Y. & Fang, X. Stress sensing and response through biomolecular condensates in plants. *Plant Commun* **6**, 101225 (2025).

10 Yu, B., Chao, D. Y. & Zhao, Y. How plants sense and respond to osmotic stress. *J Integr Plant Biol* **66**, 394–423 (2024).

11 Wang, B. *et al.* Condensation of SEUSS promotes hyperosmotic stress tolerance in Arabidopsis. *Nat Chem Biol* **18**, 1361–1369 (2022).

12 Wang, Z. *et al.* A cytoplasmic osmosensing mechanism mediated by molecular crowding-sensitive DCP5. *Science* **386**, eadk9067 (2024).

13 Ceriotti, M. *et al.* Nuclear Quantum Effects in Water and Aqueous Systems: Experiment, Theory, and Current Challenges. *Chem Rev* **116**, 7529–7550 (2016).

14 Giubertoni, G., Bonn, M. & Woutersen, S. D(2)O as an Imperfect Replacement for H(2)O: Problem or Opportunity for Protein Research? *J Phys Chem B* **127**, 8086–8094 (2023).

15 Tempra, C., Chamorro, V. C. & Jungwirth, P. Effects of water deuteration on thermodynamic and structural properties of proteins and biomembranes. *J Phys Chem B* **127**, 1138–1143 (2023).

16 Bielskute, S. *et al.* Low amounts of heavy water increase the phase separation propensity of a fragment of the androgen receptor activation domain. *Protein Sci* **30**, 1427–1437, doi:10.1002/pro.4110 (2021).

17 Reslan, M. & Kayser, V. The effect of deuterium oxide on the conformational stability and aggregation of bovine serum albumin. *Pharm Dev Technol* **23**, 1030–1036, doi:10.1080/10837450.2016.1268157 (2018).

18 Zhang, H. *et al.* Large-scale identification of potential phase separation proteins from plants using a cell-free system. *Mol Plant* **16**, 310–313 (2023).

19 Fabregas, N., Yoshida, T. & Fernie, A. R. Role of Raf-like kinases in SnRK2 activation and osmotic stress response in plants. *Nat Commun* **11**, 6184 (2020).

20 Doan, L. C., Dahanayake, J. N., Mitchell-Koch, K. R., Singh, A. K. & Vinh, N. Q. Probing Adaptation of Hydration and Protein Dynamics to Temperature. *ACS Omega* **7**, 22020–22031 (2022).

21 Denay, G., Vachon, G., Dumas, R., Zubieta, C. & Parcy, F. Plant SAM-Domain Proteins Start to Reveal Their Roles. *Trends Plant Sci* **22**, 718–725 (2017).

22 Seif, E. *et al.* Phase separation by the polyhomeotic sterile alpha motif compartmentalizes Polycomb Group proteins and enhances their activity. *Nat Commun* **11**, 5609 (2020).

23 Bienz, M. Head-to-Tail Polymerization in the Assembly of Biomolecular Condensates. *Cell* **182**, 799–811 (2020).

24 Xu, X., Fonseca de Lima, C. F., Vu, L. D. & De Smet, I. When drought meets heat - a plant omics perspective. *Front Plant Sci* **14**, 1250878 (2023).

25 Andre, A. A. M. & Spruijt, E. Liquid-Liquid Phase Separation in Crowded Environments. *Int J Mol Sci* **21**, 5908 (2020).

26 Leng, C. *et al.* Probing the Surface Hydration of Nonfouling Zwitterionic and PEG Materials in Contact with Proteins. *ACS Appl Mater Interfaces* **7**, 16881–16888 (2015).

27 Vincenzi, M., Mercurio, F. A. & Leone, M. About TFE: Old and New Findings. *Curr Protein Pept Sci* **20**, 425–451 (2019).

28 Wang, Y. *et al.* Biomolecular condensates mediate bending and scission of endosome membranes. *Nature* **634**, 1204–1210 (2024).

29 Makan, A. C., Spallek, M. J., du Toit, M., Klein, T. & Pasch, H. Advanced analysis of polymer emulsions: Particle size and particle size distribution by field-flow fractionation and dynamic light scattering. *J Chromatogr A* **1442**, 94–106 (2016).

30 Some, D., Amartely, H., Tsadok, A. & Lebendiker, M. Characterization of Proteins by Size-Exclusion Chromatography Coupled to Multi-Angle Light Scattering (SEC-MALS). *J Vis Exp*, e59615 (2019).

31 van Dop, M. *et al.* DIX Domain Polymerization Drives Assembly of Plant Cell Polarity Complexes. *Cell* **180**, 427–439 (2020).

32 Fossat, M. J., Zeng, X. & Pappu, R. V. Uncovering Differences in Hydration Free Energies and Structures for Model Compound Mimics of Charged Side Chains of Amino Acids. *J Phys Chem B* **125**, 4148–4161 (2021).

33 Laage, D., Elsaesser, T. & Hynes, J. T. Water Dynamics in the Hydration Shells of Biomolecules. *Chem Rev* **117**, 10694–10725 (2017).

34 Dai, Y. *et al.* Interface of biomolecular condensates modulates redox reactions. *Chem* **9**, 1594–1609 (2023).

35 Zhu, L., Pan, Y., Hua, Z., Liu, Y. & Zhang, X. Ionic Effect on the Microenvironment of Biomolecular Condensates. *J Am Chem Soc* **146**, 14307–14317 (2024).

36 Ye, S. *et al.* Micropolarity governs the structural organization of biomolecular condensates. *Nat Chem Biol* **20**, 443–451 (2024).

37 Kagale, S. *et al.* The emerging biofuel crop Camelina sativa retains a highly undifferentiated hexaploid genome structure. *Nat Commun* **5**, 3706 (2014).

38 Kohler, A. & Hurt, E. Exporting RNA from the nucleus to the cytoplasm. *Nat Rev Mol Cell Biol* **8**, 761–773 (2007).

39 Singh, G., Pratt, G., Yeo, G. W. & Moore, M. J. The Clothes Make the mRNA: Past and Present Trends in mRNP Fashion. *Annu Rev Biochem* **84**, 325–354 (2015).

40 Pacheco-Fiallos, B. *et al.* mRNA recognition and packaging by the human transcription–export complex. *Nature* **616**, 828–835, doi:10.1038/s41586-023-05904-0 (2023).

41 Beck, M. & Hurt, E. The nuclear pore complex: understanding its function through structural insight. *Nat Rev Mol Cell Biol* **18**, 73–89 (2017).

42 Pfaff, C. *et al.* ALY RNA-Binding Proteins Are Required for Nucleocytosolic mRNA Transport and Modulate Plant Growth and Development. *Plant Physiol* **177**, 226–240 (2018).

43 Koroleva, O. A. *et al.* Dynamic behavior of Arabidopsis eIF4A-III, putative core protein of exon junction complex: fast relocation to nucleolus and splicing speckles under hypoxia. *Plant Cell* **21**, 1592–1606 (2009).

44 Feric, M. *et al.* Coexisting Liquid Phases Underlie Nucleolar Subcompartments. *Cell* **165**, 1686–1697 (2016).

45 Mukherjee, S. & Schafer, L. V. Thermodynamic forces from protein and water govern condensate formation of an intrinsically disordered protein domain. *Nat Commun* **14**, 5892 (2023).

46 Banani, S. F., Lee, H. O., Hyman, A. A. & Rosen, M. K. Biomolecular condensates: organizers of cellular biochemistry. *Nat Rev Mol Cell Biol* **18**, 285–298 (2017).

47 Pakos-Zebrucka, K. *et al.* The integrated stress response. *EMBO Rep* **17**, 1374–1395 (2016).

48 Tom Maniatis, R. R. An extensive network of coupling among gene expression machines. *Nature* **416**, 499–506, doi:10.1038/416499a (2002).

49 Zander, G. *et al.* mRNA quality control is bypassed for immediate export of stress-responsive transcripts. *Nature* **540**, 593–596, doi:10.1038/nature20572 (2016).

50 Zhang, H., Zhao, Y. & Zhu, J. K. Thriving under Stress: How Plants Balance Growth and the Stress Response. *Dev Cell* **55**, 529–543 (2020).

Acknowledgement

We thank Dr. Susan Duncan for technical assistance in smFISH experiment, Dr. Zhaoxing Wang for providing technical assistance for SEC-MALS, Dr. Jinyu Wang for assistance in imaging. This work was funded by grants from the Ministry of Science and Technology of China (grant no. 2022YFA1303400), National Natural Science Foundation of China (grant nos. 32450060 and 22203055), and Pillars of the Nation Funding for Life Sciences at Tsinghua University to X.F., National Natural Science Foundation of China (grant no. 32200230) to Y.W., National Natural Science Foundation of China (22494700, 22494702, 22477102), Zhejiang Provincial Key Laboratory Construction Project, and Westlake Laboratory of Life Sciences and Biomedicine (2024SSYS0035) to X.Z., and National Natural Science Foundation of China (grant no. 224B2706) to L.Z.

Author contributions

X.F. conceived, guided, and supervised the project; Y.W. performed all experiments except for micropolarity measurement; Y.Y helped with the in vitro phase separation assay. L.Z. and X.Z. performed in vitro micropolarity measurement; X.L. helped with phenotypic analysis; X.F. and Y.W. together wrote the manuscript. All authors discussed the results and reviewed the manuscript.

Data Availability

All data are available in the main text or the supplementary materials. The mRNAseq and ribo-seq raw data are available at Zenodo (https://doi.org/10.5281/zenodo.17009028 and https://doi.org/10.5281/zenodo.16973647).

Competing interests

The authors declare no competing interests.

Correspondence and requests for materials should be addressed to X.F.

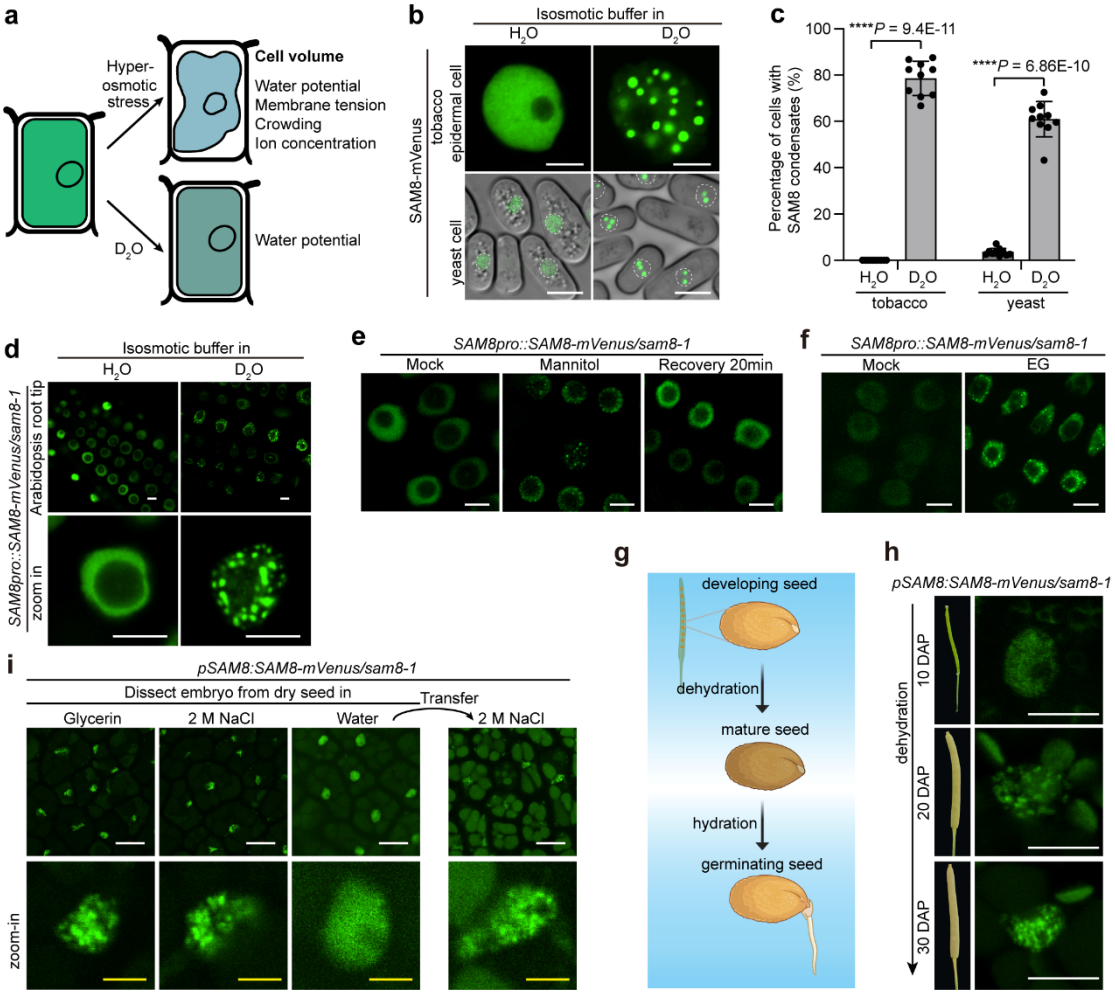

Figure 1 | SAM8 undergoes water potential-dependent condensation in vivo.

a, Illustration of the impact of osmotic stress and D_2O on plant cells. **b**, Representative confocal images of tobacco epidermal cells (top) or *Schizosaccharomyces pombe* cells (bottom) expressing SAM8-GFP. The cells were treated for 10 min with an isosmotic buffer prepared with H_2O or 90% D_2O. The white dotted circles indicate the nuclei of yeast cells**.** Scale bars, 5 μm. **c**, Quantification of the percentage of cells containing SAM8 condensates as indicated. Error bars indicate mean ± SD (n = 10). **d**, Representative confocal images of Arabidopsis root tip cells that were treated with isosmotic buffer prepared with H_2O or 90% D_2O. Scale bars, 5 μm. **e**, **f**, Representative confocal images of Arabidopsis root tip cells expressing SAM8-mVenus. The cells were treated with 0.3 M Mannitol or 0.5 M EG for 10 min. Scale bars, 5 μm. **g**, Illustration of the dehydration and hydration process during seed development and germination. **h,** Representative confocal images of embryos dissected from the different stages of seeds expressing SAM8. DAP, days after pollination. Scale bars, 5 μm. **i,** Representative confocal images of embryos dissected from the dry and imbibed seeds expressing SAM8. Scale bars: white, 10 μm; yellow, 2 μm. Representative images of *n* independent experiments (*n* = 3 (d-f, h, and i)). Asterisks indicate significant differences (two-tailed *t* test).

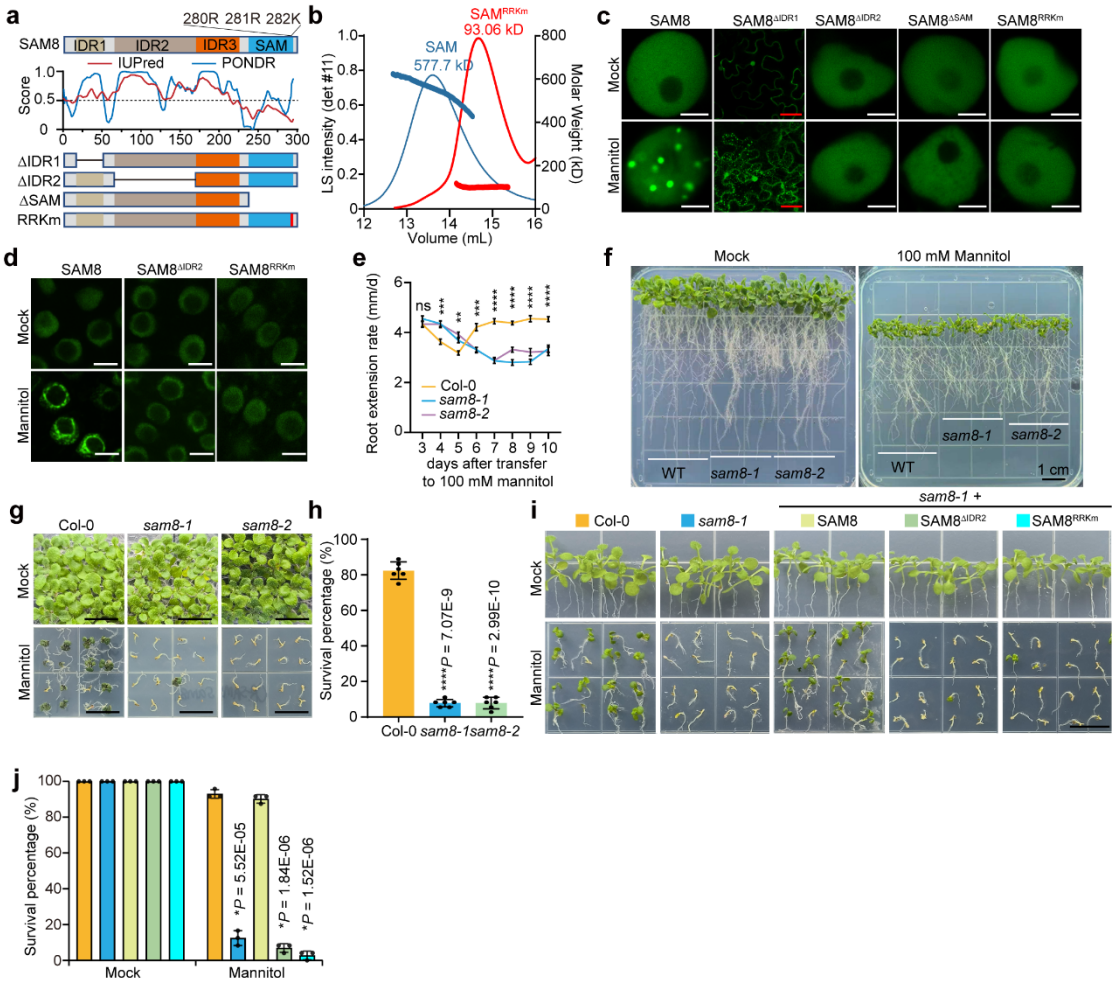

Figure 2 | SAM8 condensation is required for hyperosmotic tolerance.

a, Top and Bottom, domain structures of SAM8 and its variants. IDR, intrinsically disorder region. Middle, IDR prediction by indicate algorithms. **b**, SEC-MALS assay showing the size of the SAM domain and SAM^{RRKm}. Both proteins were fused with MBP tag to prevent misfolding. Left y-axis, the light scattering intensity from the 90° detector (detector 11). Right y-axis, molecular weight. **c**, Representative confocal images of tobacco epidermal cells expressing SAM8 and its variants. The cells were treated with or without 0.3 M mannitol. Scale bars: white, 5 μm; red, 50 μm. **d,** Representative confocal images of Arabidopsis root tip cells expressing SAM8 and variants treated with or without 0.3 M mannitol for 10 min. Scale bars, 5 μm. **e**, Quantification of the root extension rate of Arabidopsis seedlings that were transferred to medium supplemented with 100 mM mannitol. Error bars indicate mean ± SE (n = 30). Asterisks indicate significant differences (two-tailed *t* test). ns, not significant. **f,** Representative images of Arabidopsis seedlings that grew for 10 days upon transferring to medium supplemented with or without 100 mM mannitol. Scale bars, 1 cm. **g**, Representative images of 12-day-old seedlings of the indicated genotypes grown on medium containing 300 mM mannitol. Scale bar, 1 cm. **h**, Quantification of the survival percentage shown in (g). Error bars indicate mean ± SD (n = 6 replicates with each replicate containing 36 plants). **i**,

675 Representative images of 12-day-old seedlings of indicated genotypes on
676 medium containing 300 mM mannitol. Scale bar, 1 cm. **j**, Quantification of
677 survival percentage shown in (i). Error bars indicate mean ± SD (n = 3 with each
678 replicate containing approximately 24 plants). Asterisks indicate significant
679 differences (two-tailed *t* test). ns, not significant.

680

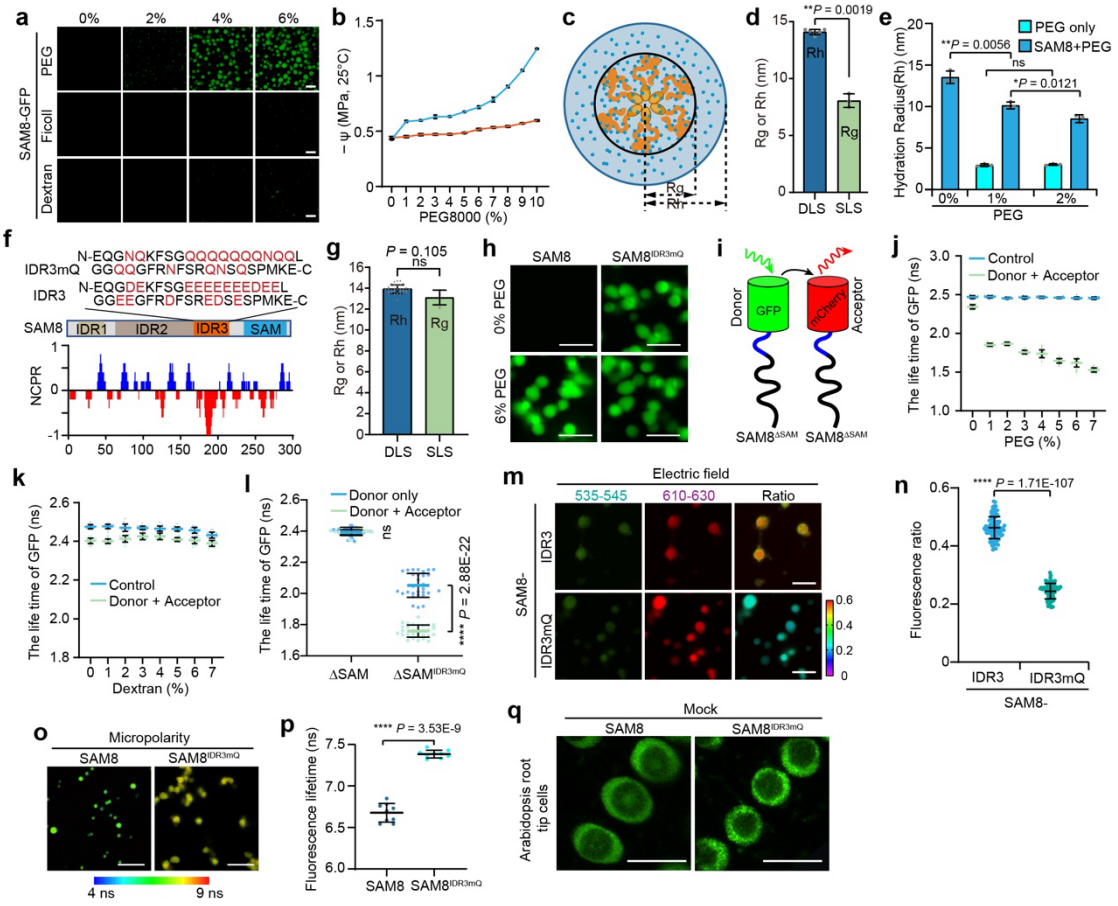

Figure 3 | The molecular basis of water potential sensing by SAM8.

a, In vitro phase separation assay of 2.5 μM SAM8 in the presence of indicated concentrations of crowders. **b,** Vapour-pressure osmometry measurement of the osmotic potential. (n = 5). **c**, Illustration of the hydration radius (Rh) and gyration radius (Rg). **d**, Measurement of Rg and Rh of SAM8. (n = 6 for DLS, n = 3 for SLS). **e**, DLS measurement of the hydration radius of the indicated solutions. (n =3). **f**, Top, the amino acid sequence of IDR3 or IDR3mQ. Bottom, the net charge per residue of SAM8 as predicted by CIDER webserver. **g**, Measurement of Rh and Rg of SAM8^{IDR3mQ}. (n = 30 for DLS and n = 3 for SLS). **h,** In vitro phase separation assay of 2.5 μM SAM8 and SAM8^{IDR3mQ}. **i**, Illustration of FLIM-FRET to test the intermolecular interactions. **j**, **k**, The lifetime of donor GFP for the indicated proteins in the presence of the indicated concentrations of PEG 8000 (j) or Dextran (k). GFP and mCherry act as negative controls. (n = 20). **l**, The lifetime of donor GFP for the indicated proteins. (n = 30). **m**, Confocal imaging of 5 μM SAM8 and SAM8^{IDR3mQ} in the presence of DI-4-ANEPPS dye. **n**, The ratio of emission at 535–545 and 610–640 nm shown in (m). (n = 98 condensates). **o**, FLIM images of dual SBD-labeled SAM8 and SAM8^{IDR3m} condensates. **p**, Quantification of the life time of dual SBD shown in (o). (n = 9). Asterisks indicate significant differences (two-tailed *t* test). ns, not significant. **q**, Confocal image of Arabidopsis root cells expressing SAM8 and SAM8^{IDR3m} in *sam8* mutant background. For (b-e, g, j-l,

703 n and p), Error bars indicate mean ± SD. Scale bars, 10 μm (a, m and o), 5 μm
704 (h, q).

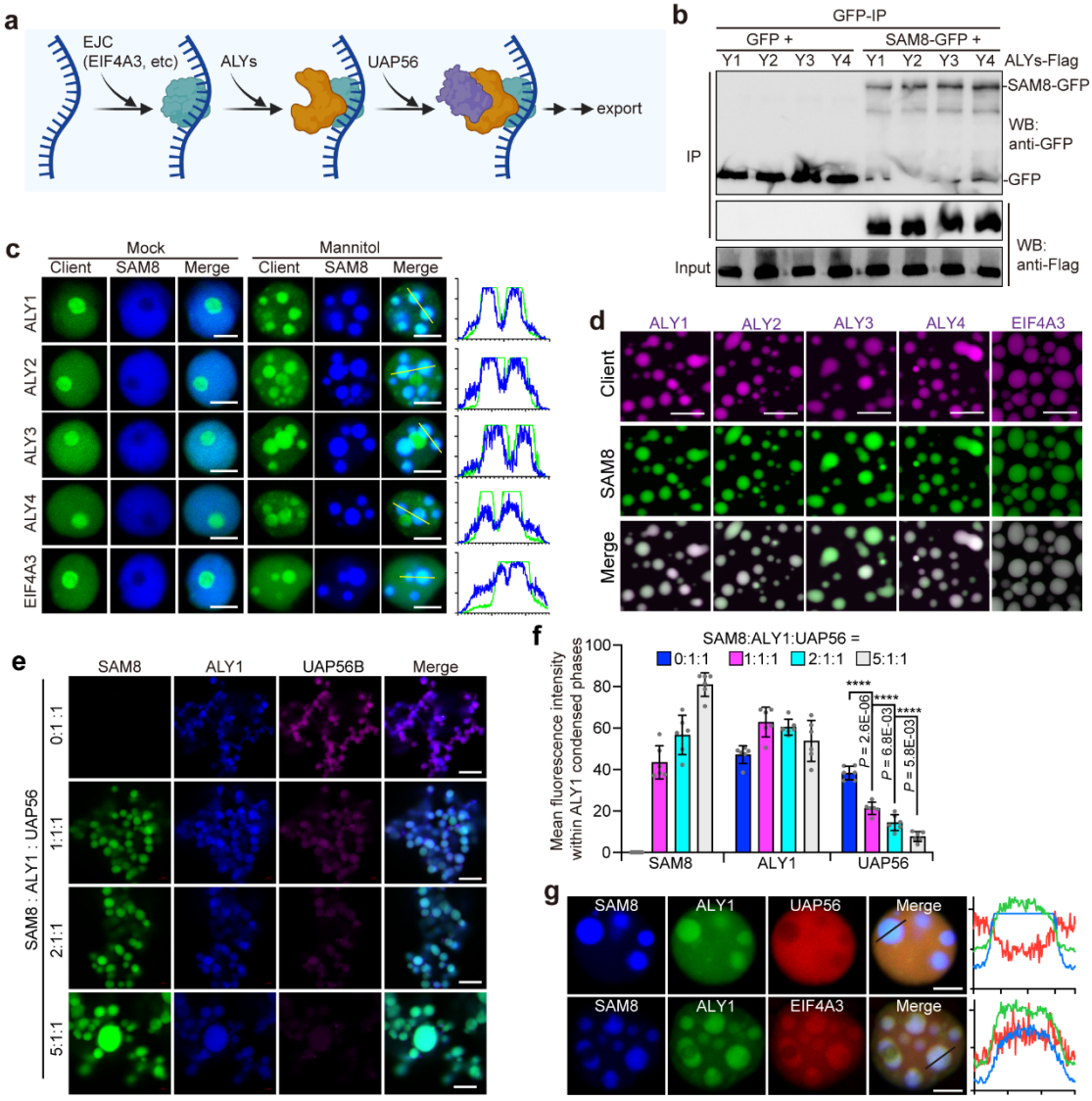

Figure 4 | SAM8 condensates selectively partition RNA export factors. **a**, Schematic illustration of the key steps of RNA export. **b**, Co-IP analyses of the interactions between SAM8 and ALYs upon co-expression in tobacco epidermal cells. For gel source data, see Supplementary Figure 1. **c**, Representative confocal images showing the colocalization of ALYs-GFP with SAM8-Cerulean condensates. Scale bars, 5 μm. **d**, In vitro phase separation assay showing the colocalization of ALY1 with SAM8 droplets. Scale bars, 5 μm. **e,** In vitro phase separation of 2.5 μM ALY1-BFP and UAP56B-mCherry in the presence of increasing amounts of SAM8-GFP (0, 2.5, 5 and 12.5 μM, respectively). Scale bars, 5 μm. **f,** The mean fluorescence intensity inside droplets shown in (g). Error bars indicate mean ± SD (n= 6 independent experiments). Asterisks indicate significant differences (two-tailed *t* test). **g**, Co-expression in tobacco epidermal cells showing that SAM8 condensates enrich ALY1 and EIF4A3 but exclude UAP56B. Scale bars, 5 μm. Fluorescence plots were shown at right.

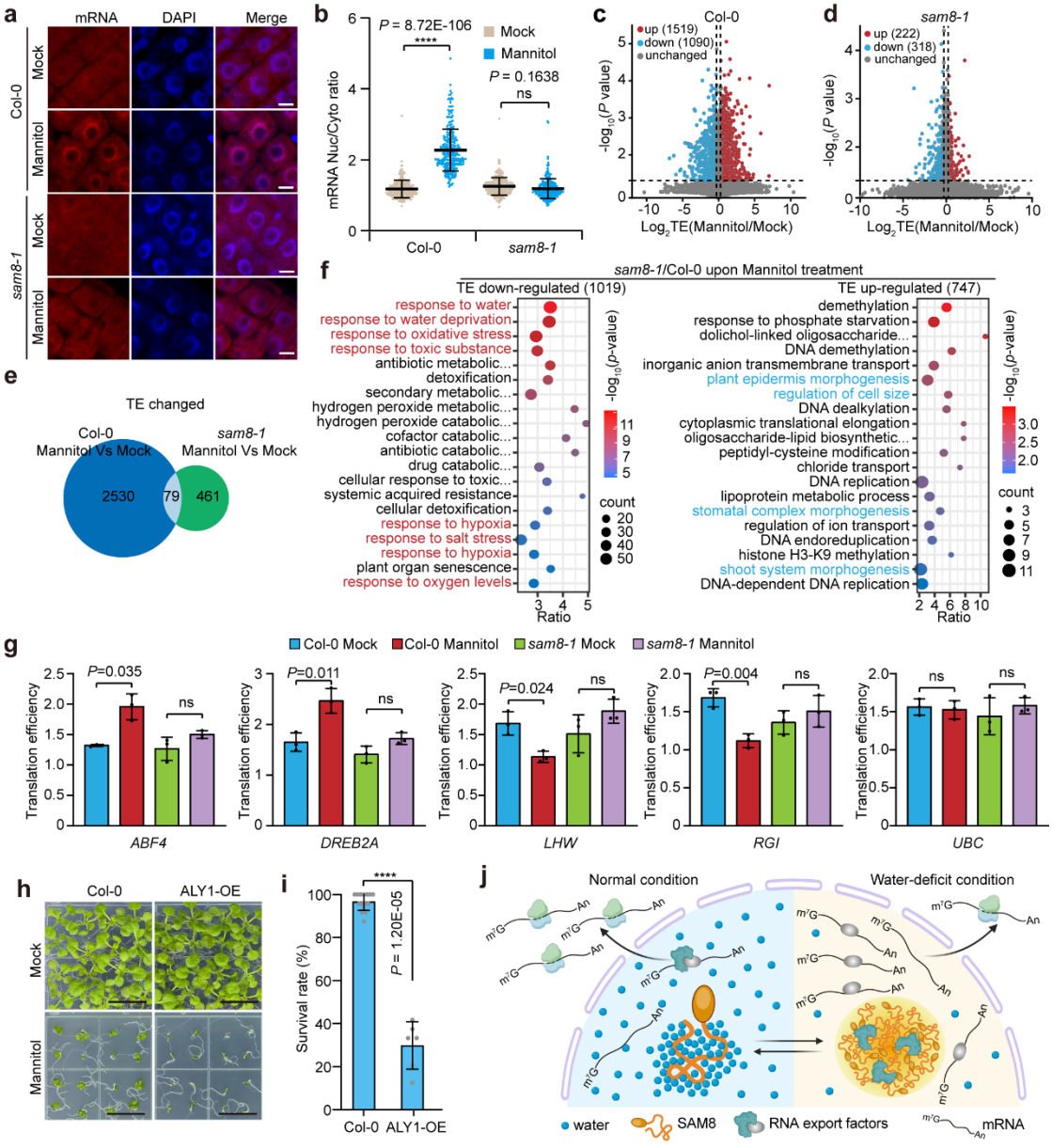

721

722 **Figure 5 | SAM8 condensation suppresses mRNA export and reprograms**
723 **translation under osmotic stress.**
724 **a**, RNA FISH with oligodT probes in Arabidopsis root tips under mock and
725 osmotic stress conditions. Scale bars, 5 μm. **b**, Quantification of the nuclear-to-
726 cytoplasmic ratio of mRNA signal shown in (a). Error bars indicate mean ± SD
727 (n = 271, 292, 288, and 297 cells, respectively). Asterisks indicate significant
728 differences (one-way ANOVA followed by the least significant difference test).
729 ns, not significant. **c**, **d**, Volcano plot showing the translation efficiency (TE)
730 change in Col-0 (c) and *sam8-1* (d) under mannitol treatment compared to mock.
731 **e**, Venn diagrams showing the overlap of TE changed genes in Col-0 and
732 *sam8-1*. **f**, Top 20 enriched GO terms for TE up- and down-regulated genes in
733 *sam8-1* versus Col-0 under mannitol treatment. Stress- and development-
734 related items are highlighted in red and blue, respectively. **g**, Translation
735 efficiency of candidate genes as determined by polysome profiling. *UBC10*

served as a control. Error bars indicate mean ± SD (n = 3). Asterisks indicate significant differences (two-tailed *t* test). ns, not significant. **h**, Representative images of 12-day-old seedlings of indicated genotypes grown on medium containing 300 mM mannitol. Scale bars, 1 cm. **i**, Quantification of survival percentage shown in (h). Error bars indicate mean ± SD (n = 6 replicates with each replicate containing approximately 24 plants). Asterisks indicate significant differences (two-tailed *t* test). **j**, A working model for SAM8. Under normal growth conditions, when cellular water is enough to keep SAM8 hydrated, SAM8 condensation is inhibited. Once cellular water content is reduced upon encountering water-deficit stress, SAM8 hydration is decreased, activating SAM8 condensation. SAM8 condensates selectively include and exclude RNA export factors, thereby disrupting mRNA export and resulting in translation reprogramming.

Materials and Methods

Plant materials and growth conditions and stress treatment

All the Arabidopsis thaliana mutants and transgenic plants used in this study were in the Columbia (Col-0) background. The T-DNA insertion mutant *sam8-1* (SALK_065676) was ordered from the AraShare. *sam8-2* is a CRISPR-generated allele carrying a 1-bp insertion 39 bp downstream of the start codon, which introduces a frameshift and premature stop codon. The resulting protein is: MAELQLVEGHQINRRFYPAGDNKLNRSTGNIRRSRSFSRIETIEKT*. The *ok130-null* mutant was kindly provided by Prof. Pengcheng Wang (Southern University of Science and Technology). Seeds were surface sterilized with 2.5% (v/v) sodium hypochlorite and 70% (v/v) ethanol, stratified for 3 days in the dark at 4°C, and sown on half-strength Murashige and Skoog (MS), 0.8% (w/v) agar plates supplemented with 1% (w/v) sucrose. Plate media were transferred to a growth chamber under a long-day (16 h light 22°C/8 h dark 18°C) photoperiod.

For the germination kinetic assay, all seeds of the indicated geneotypes were harvested on the same date from plants grown under identical conditions. They were then uniformly dried at 37 °C for 2 weeks to ensure a consistent after-ripening process. Subsequently, seeds were sown on the same batch of medium and placed in a growth chamber without stratification under a long-day photoperiod (16 h light at 22 °C / 8 h dark at 18 °C). Germination rate was rated as the mean percentage of seeds that had ruptured their seed coats. Each genotype was evaluated in three biological replicates, with each replicate consisting of approximately 300 seeds.

For direct osmotic stress treatment, sterilized seeds of different genotypes were germinated on 1/2 MS medium supplemented with 300 mM D-Mannitol (Solarbio, M8141) and grown at 22°C or 26°C. The phenotypes were recorded at 12 days post germination. The survival was determined based on the ability of seedlings to resume growth after stress removal. Specifically, seedlings were transferred back to 1/2 MS medium following stress treatment, and survival was scored 7 days later. Seedlings that remained green and produced new tissues (e.g., true leaves) were counted as survivors, whereas those that became white or brown and failed to resume growth were scored as non-survivors. For transfer assay, sterilized seeds of Col-0 and *sam8-1* were germinated on standard half-strength MS medium at 22°C for 3 days, then transferred to medium containing 750 mM D-Mannitol and grown vertically at 22°C or 26°C for 5 days. After treatment, those seedlings were transferred back to a normal medium and grown at 22°C for 10 days before recording phenotypes.

For the root extension assay, 5-day-old seedlings grown on standard half-strength MS medium were transferred to medium containing mannitol and grown vertically for 10 days. For meristem zone measurement, the seedlings were imaged under DIC of a Nikon AXR with NSPARC confocal microscope system using a ×100/1.45 oil objective 2 days after transfer. The length of the meristem zone was quantified from the QC (Quiescent Center) to the first

elongated cell. For the extension rate analysis, root length was measured every day, and the rate was calculated as millimeters per day.

Plasmid construction

To generate the *pSAM8::SAM8-mVenus* construct, a 2.2-kb promoter and a 1-kb 3' untranslated region (UTR) were amplified from wild-type Col-0 genomic DNA and cloned into the pCAMBIA1300-mVenus vector[1], giving rise to the *pSAM8::mVenus-UTR* construct. The coding sequence of SAM8 was amplified and inserted between the promoter and mVenus. For SAM8 variants, site-directed mutagenesis or domain deletion was performed with a standard two-step polymerase chain reaction (PCR) and verified by DNA sequencing to generate the coding sequences of SAM8$^{\Delta IDR1}$, SAM8$^{\Delta IDR2}$, SAM8^{IDR3mQ}, SAM8^{IDR3mS}, SAM8^{IDR3mK}, SAM8^{IDR3mR}, SAM8$^{\Delta SAM}$, and SAM8^{RRKm}. All coding sequences were cloned into the *pSAM8::mVenus-UTR* vector.

To generate *sam8-2* mutant, two sgRNAs were designed and inserted into the *Bbs*I sites of the pAtU6-26-M vector. The Cas9 cassettes were subcloned into pCambia1300-UBQ:Cas9-P2A-GFP-rbcS-E9t vector[2] (digested with *Kpn*I and *EcoR*I). All constructs were introduced into *Agrobacterium tumefaciens* strain GV3101 and transformed into *sam8-1* mutant plants via the standard floral dipping method. Positive transformants were selected on half-strength MS medium containing 30 mg/L hygromycin (AMRESCO, K547). Homozygous transgenic lines were used for experiments. For the *sam8-2* mutant, Cas9-free plants were used for experiments.

For the constructs used in transient expression in tobacco epidermal cells, the coding sequences of SAM8 and its variants, ALY1/2/3/4, eIF4A3, and UAP56B, and NUL1 were amplified and inserted into the pCAMBIA1300-35S-mVenus/ NmVenus/CmVenus/Flag/mCerulean/mCherry vector[1] (digested with KpnI). The same construct was used for generating overexpression transgenic lines where necessary.

To generate the constructs used for heterologous expression in yeast cells, the coding sequences of SAM8 and its variants were amplified and inserted into the pDUAL-Pnmt1-yeGFP vector[3] (digested with NheI and BamHI).

To generate the constructs used for in vitro protein expression, the coding sequences of SAM8 and its variants, ALY1/2/3/4, eIF4A3, UAP56B, SAM7, and SOSEKI1 were amplified and inserted into the pET11-6×His, pET11-6×His-GFP, pET11-6×His-mCherry, or pET11-6×His-BFP expression vector[4] (digested with NheI). Where necessary, a maltose-binding protein (MBP) solubility tag was placed at the N-terminus of the construct, followed by a tobacco etch virus protease (TEV) cleavage site. To generate the constructs used for micropolarity assay, the coding sequences of MBP-SAM8 or MBP-SAM8^{IDR3mQ} were amplified and inserted into the p1-Halo-pET29b expression vector (digested with NheI and BamHI).

All cloning was performed using the ClonExpress II One Step Cloning kit (Vazyme, C115). The Primer sequences used in this study are provided in Supplementary Table 3.

In vitro Protein expression and purification

All proteins were expressed and purified from *Escherichia coli* (Rosetta) cells using Ni-NTA resin as described previously[5]. Briefly, protein expression was induced by 0.4 mM isopropyl-β-D-1-thiogalactopyranoside (IPTG) at 15°C overnight. Cells were collected by centrifugation and re-suspended in lysis buffer (40 mM Tris-HCl pH7.4, 500 mM NaCl, 10% glycerol). The suspension was sonicated for 20 min (3 s ON, 6 s OFF, SCIENTZ) and centrifuged at 12,000 *g* for 60 min at 4°C. The supernatant was incubated with Ni-NTA agarose for 20 min and washed five times with wash buffer (40 mM Tris-HCl pH7.4, 500 mM NaCl, 20 mM Imidazole) and eluted with elution buffer (40 mM Tris-HCl pH7.4, 500 mM NaCl, 500 mM Imidazole). Proteins were purified by gel filtration chromatography (Superdex-200; GE Healthcare) and stored in the buffer (40 mM Tris-HCl pH7.4, 500 mM NaCl, 1 mM DTT) at 4°C.

SEC-MALS

Size-exclusion chromatography coupled with a multi-angle laser light scattering (SEC-MALS) was performed as described previously[6]. Briefly, chromatography was performed in 40 mM Tris-HCl pH7.4 and 500 mM NaCl using a Superdex-200 10/300 GL size exclusion column (GE Healthcare). The concentrations of MBP-SAM, MBP-SAM^{RRKm}, MBP-SAM8, MBP-SAM7, and MBP-SOSKEI1 used for this assay are 2 mg/mL, 2 mg/mL, 5 mg/mL, and 5 mg/mL, respectively. The chromatography system was connected to a Wyatt DAWN HELEOS laser photometer and a Wyatt Optilab T-rEX differential refractometer. Wyatt ASTRA 7.3.2 software was used for data analysis.

Dynamic Light Scattering (DLS) measurement

SAM8 protein of 2 mg/mL in 40 mM Tris-HCl pH 7.4, 100 mM NaCl was used for DLS measurement. The protein sample of 100 µL was transferred into a quartz cuvette (WYATT, JC-0247). DLS measurements were performed using DynaPro NanoStar (Wyatt). Each data point was collected from 10 to 30 acquisitions. The data were analyzed in the DYNAMICS software using a cumulant fit to the autocorrelation function.

Yeast transformation for heterologous expression

The plasmids were linearized with NotI and the resulting fragments were gel-purified and transformed into the fission yeast strain LD328 (genotype his3-D1 leu1-32) as described previously[7]. Briefly, yeast cells were cultured until the OD600 reached 0.4-0.8. For each reaction, 500 µL cultured cells were collected, washed three times with sterilized water and resuspended in buffer I (240 µL of 50% PEG3350, 36 µL of 1.0 M LiAc and 50 µL of 2.0 mg/mL carrier DNA). The linearized DNA (34 µL, up to 1 µg) was added to the resuspended cells, mixed vigorously and incubated at 42°C for 40 min. The cells were collected and

resuspended in 100 μL water and plated on EMM + HT (EMM medium supplemented with 45 mg/L histidine and 15 μM thiamine) plates. After incubation at 30°C for 2-3 days, individual colonies were selected on EMM + H (EMM medium supplemented with 45 mg/L histidine) plates. The cells were used for subsequent imaging analyses.

Fluorescence imaging of cells and tissues

Five-day-old Arabidopsis seedlings or tobacco leaves were soaked in liquid half-strength MS medium supplemented with or without D-Mannitol, PEG8000, EG, or isosmotic buffer prepared with heavy water (SIGMA, 151882). After treatment, the root tip or a small leaf disc was mounted on a slide, covered with a coverslip and immediately imaged under a Zeiss LSM880 confocal microscope using a ×100/1.40 oil objective or Nikon AXR with NSPARC confocal microscope system using a ×100/1.45 oil objective. GFP was excited at 488 nm and detected at 491-535 nm; mVenus was excited at 514 nm and detected at 529-570 nm, mCherry was excited at 561 nm and detected at 575-625 nm, mCerulean or BFP was excited at 405 and detected at 410-507 nm. The channels of mVenus, mCerulean, and mCherry were acquired sequentially to avoid emission crosstalk.

For imaging of SAM8 during seed development, developing siliques from *pSAM8::SAM8-mVenus/sam8-1* plants were collected. The seeds were dissected to remove their seed coats and then imaged. For imaging of SAM8 during seed germination, dry seeds were imbibed in either glycerin or in solutions of NaCl or water for 10-20 min and dissected to remove the seed coats. The embryos were mounted on a slide, covered with a coverslip, and immediately imaged under a Nikon AXR with NSPARC confocal microscope system using a ×100/1.45 oil objective.

For imaging of yeast cells, three colonies were streaked on a medium plate and cultured overnight. Before imaging, a colony was resuspended in liquid medium containing or not containing 1.2 M sorbitol or 0.6 M NaCl. The cells were sprayed onto a slide and covered with a coverslip. Imaging was performed on a Zeiss LSM880 confocal laser microscope. GFP was excited at 488 nm and detected at 491-535 nm. Imaging at 35°C was performed on Nikon AX R confocal microscope equipped with Okolab microscope incubator using 40× 0.95-NA objective.

In vitro phase separation assay

For in vitro phase separation, the solubility tag MBP was removed by TEV protease cleavage. The proteins were diluted to desired concentrations with indicated ionic strengths. The protein samples were incubated for 30 min before imaging. For D_2O treatment, the same buffer was prepared with heavy water (SIGMA, 151882). To analyze the effect of PEG8000, Dextran 40 and Ficoll 400 on SAM8 phase separation, indicated concentrations of those crowders were added to the protein samples in 40 mM Tris-HCl pH 7.4, 150 mM NaCl

and incubated at the indicated temperatures. Protein samples were imaged in a 384-well low-binding microscopy plate (Greiner bio-one, 781090) using a Zeiss LSM880 confocal microscope equipped with a ×63/1.40-NA oil objective. The quantification of mean intensity and droplet sizes and numbers was performed using ImageJ.

Measurement of the electric field

The electric field was measured using Di-4-ANEPPS as previously described[8]. Briefly, Di-4-ANEPPS (ThermoFisher) was mixed with protein samples with a final concentration of 1 μM before imaging. Confocal fluorescence images were performed on a Nikon AXR confocal microscope equipped with a 100× 1.49-NA objective. The fluorescence was excited at 470 nm and collected at both 535-545 nm and 610-640 nm. The electrical potential of condensates was calculated as the fluorescence ratio of 535-545 nm and 610-640 nm of the same condensate.

Micropolarity measurement

The proteins were mixed in a 1:1 molar ratio with Halo-SBD and incubated overnight at room temperature in 40 mM Tris-HCl and 500 mM NaCl. Unlabelled dye was removed using a PD MidiTrap G-25 desalting column (Cytiva). The labelled protein was then mixed with the unlabeled protein to achieve a labeling ratio of approximately 10% to minimize potential fluorophore-induced artifacts. The mixed protein sample was treated with 1 μM TEV protease to remove the MBP tag and diluted to a final concentration of 5 μM. PEG8000 of a final concentration of 6% was added to the protein sample. An aliquot of 10 μL was transferred to the glass slide with a 500-μm spacer. A cover slip (0.17 mm) was placed on the top of the spacer. The slide was inverted and allowed to settle for 30–60 minutes before FLIM imaging. FLIM was performed using a Leica STELLARIS 8 FALCON microscope equipped with a pulsed white laser (WLL) using ×63 oil-immersion objective (Leica, HC PL Apo 63×/1.40 oil CS2). The SBD was excited at 448 nm with 10 MHz rate. The fluorescence lifetime fitting and image analysis were performed using LAS X software.

Fluorescence lifetime imaging-förster resonance energy transfer (FLIM-FRET)

Proteins at a final concentration of 2.5 μM were diluted in 384-well microscopy plates and incubated for 30 minutes before imaging. FLIM-FRET was performed using a Leica TCS SP8 laser-scanning confocal microscope equipped with a 100×/1.40-NA oil immersion objective. Samples were scanned with a slow speed of 100 Hz with a repetition rate of 80 MHz. mGFP fluorescence was excited at 488 nm and detected at 500-540 nm using the in-built hybrid detector. A time-correlated single photon counting (TCSPC) system was used for recording photon events.

All FLIM data analysis was performed using Leica LAS X FLIM FCS software. The minimum threshold count of recorded photons for modeling was 100. The

recorded TCSPC photon arrival time histogram showed multi-exponential decay. Therefore, the photon arrival times were fitted to a double-exponential reconvolution function, allowing the calculation of mean lifetime by intensity weight. A minimum of 30 ROIs were selected for analysis. The lifetime of each group was calculated.

Phylogenetic analysis of SAM8

To examine the conservation of SAM8, SAM8 homologs were identified in *OrthoDB* (https://www.orthodb.org/). A total of 143 SAM8 homologs were identified, and 29 of them from representative species were subjected to Neighbor-Joining tree construction using ClustalW2. The IDRs were predicted using the IUPred2A algorithm (https://iupred2a.elte.hu/).

Fluorescence recovery after photobleaching (FRAP) assay

FRAP of SAM8 condensates was performed on a Nikon AXR confocal microscope system using a ×60/1.42 oil objective. After 1 acquisition, three ROIs corresponding to SAM8-mVenus condensates were bleached using a laser intensity of 100% at 488 nm. Recovery was recorded for every second for a total of 68 seconds after bleaching. The fluorescence intensity was measured with ImageJ.

Turbidity measurements

SAM8 and its variants were diluted to final concentration of 2.5 μM in 40 mM Tris-HCl pH 7.4, 150 mM NaCl with or without 6% PEG and transferred into flat bottom 96-well plates (Corning, 3364). Turbidity of protein samples was measured at 600 nm using VARIOSKAN FLASH (Thermo).

Quantitative RT-PCR

Total RNA was extracted from Arabidopsis seedlings or other tissues using TRIzol reagent (Invitrogen, 15596018). Contaminating DNA was removed using DNase I (Promega, M6101). Reverse transcription was performed by M-MLV reverse transcriptase (Invitrogen, 28025013) using oligo(dT) primer. Quantitative PCR reactions were performed using the Applied Biosystems® 7500 fast with 2×M5 HiPer SYBR Premix EsTaq (Mei5 Biotechnology, MF787-T) in a final volume of 20 μL. *Actin* or *UBC* was used as an internal control. The primers used for qPCR are listed in Supplementary Table 3.

Osmotic potential measurement

Vapour pressure osmometry was performed on the Vapro 5600 (ELITechGroup) system according to the manufacturer's instructions. The instrument was allowed to equilibrate to ambient temperature overnight, and the reading stability was validated before measurements were performed. Osmometry readings were assessed for solutions of varying composition and confirmed to be normally distributed with the following tests: Anderson–Darling, D'Agostino–Pearson, Shapiro–Wilk, Kolmogorov–Smirnov. For the measurement of osmotic potential in the FLIM-FRET assay, the buffer containing 40 mM Tris-HCl pH 7.4, 100 mM KCl was used to prepare PEG8000, NaCl, mannitol, or

Dextran 40 solutions. For measuring osmotic potential in the seedling treatment, a 1/2 MS liquid medium was used to prepare mannitol or PEG solutions. The water potential is calculated by osmolaritiy x R x T (R gas constant, T absolute temperature).

Immunostaining

Immunostaining of Arabidopsis root tip nuclei was performed as described previously[4]. Briefly, 7-day-old Col-0 seedlings were treated with isosmotic buffer prepared with H_2O or D_2O for 15 min and fixed immediately with 4% paraformaldehyde plus 0.1% Triton X-100 in PBS buffer by applying a brief vacuum. Samples were digested with 3% cellulase R-10 and 0.3% Macerozyme R-10 (Yakult Pharmaceutical Industry) at 37 °C for 5-10 min. Root tips were then cut and squashed on a Polysine-coated slide in a drop of PBS buffer. The slide was then blocked with blocking solution (3% bovine serum albumin in PBS buffer) and incubated with primary antibody to Flag (Abcam, ab18230) and secondary antibody (Invitrogen, A-21202). After secondary antibody incubation, a drop of DAPI Fluoromount-G (Southern Biotech) was added to each slide. The slide was sealed with a coverslip and imaged with a Nikon AXR with NSPARC confocal microscope system using a ×100/1.45 oil objective. Alexa Fluor 488 was excited at 488 nm and detected at 499–550 nm, and DAPI was excited at 405 nm and detected at 429–474 nm.

RNA fluorescence in situ hybridization (FISH)

RNA FISH was performed as previously described[9]. Roots from 7-day-old Col-0 and *sam8-1* seedlings were treated with liquid medium containing 300 mM D-Mannitol for 1 h and then fixed in 4% paraformaldehyde for 15 min at room temperature with gentle vacuum. The roots were washed twice with 1x PBS and put onto a slide and covered with a coverslip. The samples were squashed, flash-frozen for ~5 sec in liquid nitrogen and air-dried at room temperature for 30 min. The samples were then permeabilized in 70% ethanol for 2 h and washed twice with wash buffer (10% formamide, 2x SSC). A volume of 100 µL hybridization buffer (100 mg/mL dextran sulphate, 10% formamide, 2×SSC) containing 1 µM 5'-Cy5-dT35 probe was added to each slide and incubated at 45°C chamber overnight in the dark. After hybridization, the samples were washed twice in wash buffer (10% formamide, 2× SSC), incubated with 100 µL of 10 µg/mL DAPI at 37°C for 1 h in the dark, washed twice with wash buffer (10% formamide, 2x SSC) and imaged by Zeiss LSM880 microscope system using a ×100/1.45 oil objective. The probe sequences used in this study are provided in Supplementary Table 3.

Mass spectrometry and data analysis

Mass spectrometry was performed as described previously[10]. Briefly, protein samples were separated by SDS-PAGE and digested in-gel with trypsin (0.5 ng/µL). The peptides were extracted from gel slices, separated by HPLC and sprayed into an LTQ Orbitrap Elite System mass spectrometer (Thermo). A database search was performed on the MASCOT server (Matrix Science Ltd)

against the IPI (International Protein Index) Arabidopsis protein database. The relative amount of each protein was determined by label-free quantification. The data of *35S::YFP-TurboID/*Col-0 was used as a background control. Proteins with an adjusted *P*-value < 0.05 and fold change ≥ 2 were considered as being enriched by SAM8.

Co-immunoprecipitation

Approximately 5 grams of *N. benthamiana* leaves co-expressing SAM8-GFP and other Flag-tagged proteins was ground into fine powder in liquid nitrogen. The powder was lysed with 10 mL lysis buffer (20 mM Tris-HCl pH 7.4, 150 mM NaCl, 4 mM $MgCl_2$, 0.5% NP-40, 5 mM DTT, 1×protease inhibitor cocktail and 1mM PMSF) at 4°C for 30 min. After filtration through Miracloth (Millipore, 475855-1RCN) and brief centrifugation, the supernatant was incubated with 10 μL of GFP-Nanoab-Magnetic Beads (LABLEAD, GNA-50-1000) for 30 min at 4°C. The beads were washed four times with lysis buffer and boiled in SDS loading buffer. The immunoprecipitates were subjected to western blot analyses.

Western blot analysis

Protein samples were resolved by SDS-PAGE and transferred to PVDF membranes. Antibodies against GFP (11814460001, Roche) and Flag (F1804, Sigma) were used as primary antibodies. After the primary antibody incubation, horseradish peroxidase (HRP)-conjugated secondary antibodies (GE Healthcare) were used for protein detection by chemiluminescence (Thermo, 34095).

Bimolecular Fluorescence Complementation (BiFC)

BiFC assays were performed as described previously[11]. Briefly, the Agrobacterium cells were resuspended using infiltration buffer (10 mM $MgCl_2$,10 mM MES, pH 5.7, and 100 μM acetosyringone) to an OD_{600} of 1.0. The cells containing BiFC pairs were mixed in equal ratio and infiltrated into *N. benthamiana* leaves. Two days after infiltration, *N. benthamiana* leaves were imaged under a Zeiss 880 confocal microscope. The whole procedure was repeated independently at least three times.

Ribo-seq, RNA-seq and data analysis

Ten-day-old seedlings were treated with or without 300 mM D-Mannitol for 1 h and divided two groups for Ribo-seq and RNA-seq analysis, respectively. For mRNA-seq, total RNA was purified with oligodT-beads to obtain polyA+ mRNAs. RNA-seq libraries were constructed using NEXTflex RNA-Seq Kit (Bioo Scientific, USA). Briefly, RNAs were fragmented and reverse-transcribed to produce the first and second strands of cDNA. The cDNA was purified and ligated with DNA adapters. The ligated DNA was used as templates for PCR amplification using primers specific to adaptors. The resulting PCR products were purified by AMPure XP beads and used for sequencing on Illumina NovaSeq 6000. Raw sequencing data was filtered by fastp20 (version 0.19.7)

to remove low-quality reads (reads with more than 50% nucleotides having phred score ≤ 5, or reads with more than 10% unmapped nucleotides). The cleaned reads were mapped to the TAIR10 reference genome using HISAT2 (2.2.1). Read pairs were assigned to CDS of TAIR10 genes using featureCounts (2.0.6). Differential gene expression analysis was performed using the DESeq2 R package (1.42.0).

For Ribo-seq, samples were fast-frozen and ground in liquid nitrogen. The resulting fine powder was resuspended in lysis buffer (20 mM Tris-HCl pH 7.4, 150 mM NaCl, 5 mM $MgCl_2$, 1 mM DTT, 100 μg/mL cyclohexane, 1% Triton X-100, 25 U/mL DNase I). The lysate was treated with nonspecific endoribonuclease RNase I. Isolation of monosomes was performed by size-exclusion chromatography with MicroSpin S-400 HR columns (Cytiva, 27-5140-01). Ribosome protected fragments (RPFs) were isolated from monosome fractions and subjected to rRNA depletion using QIAseq FastSelect –rRNA Plant Kit (Qiagen, 334315). Following PAGE purification, the both ends of RPFs were phosphorylated and ligated with 5' and 3' adapters respectively. The purified RNA fragments were reversely transcribed to cDNAs and amplified by PCR. After library construction using NEBNext® Multiplex Small RNA Library Prep Set for Illumina® (Set 1) (NEB, E7300S), the concentration of DNA was measured by Qubit® 2.0 Fluorometer and adjusted to 1 ng/μL. After quality control of the insert size and concentration using Agilent 2100 Bioanalyzer and quantitative PCR, the library was sequenced on Illumina platform.

For ribo-seq data analysis, low-quality reads were filtered by in-house scripts. Reads mapped to rRNA and tRNA by Bowtie (version 1.1.2) were discarded. Cleaned reads were mapped to TAIR10 genome using TopHat2(2.0.12). Mapped reads were assigned to CDS of TAIR10 genes using HTSeq(0.9.1).. The fold changes of RPFs were determined by edgeR25 (version 3.24.3) using the quasi-likelihood method. Translational efficiency (TE) was calculated as the ratio of Ribo FPKM to total mRNA RPKM with FPKM ≥ 1 Genes ≥ 1.2-fold change and p value < 0.05 were identified as significantly changed genes. the clusterProfiler (4.8.1) was used for functional enrichment analyses in NovoMagic.

Ribosom profiling and Polysomal RNAs extraction

Polysome profiling was performed as previously described[12] with minor modifications. Five-day-old seedlings (~0.2 g/sample) were treated with or without 0.3 M Mannitol for 1 h and then ground into fine powder in liquid nitrogen, homogenized in 0.8 mL pre-chilled polysome extraction buffer [200 mM Tris-HCl pH 9.0, 200 mM KCl, 35 mM $MgCl_2$, 25 mM EGTA, 1% sodium deoxycholate, 1% Detergent mix (20% Briji, 20% Triton X-100, 20% Igepal CA630, 20% Tween 20), 1% Polyoxyethylene 10 tridecyl ether (PTE), 5 mM DTT, 1 mM PMSF, 50 μg/mL cycloheximide, 50 μg/mL chloramphenicol and 100U/mL RNasin ribonuclease inhibitor (Promega)], and incubated on ice for 20 min. The resulting slurry was centrifuged at 13,000 rpm, 4°C for 15 min. 100

μL of the resulting supernatant was saved for total mRNA isolation, and another 700 μL was loaded on top of a pre-chilled 10 to 50% sucrose gradient (10 × Sucrose salt buffer: 400 mM Tris-HCl pH 8.4, 200 mM KCl, 100 mM $MgCl_2$) and centrifuged in a Beckman SW41Ti rotor at 33,500 rpm for 3 h at 4°C. The absorbance of separated subunits, monosomes and polysomes was detected at UV_{260} and 14 fractions were collected using a gradient fractionator (Biocomp). Polysomal RNAs were isolated from the mixed polysomal fractions (fraction 9 to 14) using Trizol/chloroform method. The translational efficiency was calculated as the ratio of RNA level in polysomal fractions compared to total transcripts by quantitative RT-PCR.

Statistics

Statistical analysis was performed using either unpaired two-tailed Student's *t* test or one-way ANOVA that is followed by the least significant difference (LSD) test. For the Statistical significance of the interaction between two factors, Shapiro-Wilk and Levene's tests were used to assess normality and homogeneity, respectively. A two-way ANOVA with Tukey's post hoc analysis was performed (α = 0.05). Statistical details of experiments are specified in the figure legends. The fluorescence intensity was measured with ImageJ. All statistical analyses were performed in IBM SPSS Statistics v19.

Method references

1 Geng, P. *et al.* A thermosensor FUST1 primes heat-induced stress granule formation via biomolecular condensation in Arabidopsis. *Cell Res* **35**, 483–496 (2025).

2 Wang, J. & Chen, H. A novel CRISPR/Cas9 system for efficiently generating Cas9-free multiplex mutants in Arabidopsis. *aBIOTECH* **1**, 6–14 (2020).

3 Matsuyama, A. *et al.* pDUAL, a multipurpose, multicopy vector capable of chromosomal integration in fission yeast. *Yeast* **21**, 1289–1305 (2004).

4 Wang, B. *et al.* Condensation of SEUSS promotes hyperosmotic stress tolerance in Arabidopsis. *Nat Chem Biol* **18**, 1361–1369 (2022).

5 Fang, X. *et al.* Arabidopsis FLL2 promotes liquid-liquid phase separation of polyadenylation complexes. *Nature* **569**, 265–269 (2019).

6 Nichols, M. R. *et al.* Biophysical comparison of soluble amyloid-beta(1-42) protofibrils, oligomers, and protofilaments. *Biochemistry* **54**, 2193–2204 (2015).

7 Gietz, R. D. Yeast transformation by the LiAc/SS carrier DNA/PEG method. *Methods Mol Biol* **1163**, 33–44 (2014).

8 Dai, Y. *et al.* Interface of biomolecular condensates modulates redox reactions. *Chem* **9**, 1594–1609 (2023).

9 Duncan, S., Olsson, T. S. G., Hartley, M., Dean, C. & Rosa, S. Single Molecule RNA FISH in Arabidopsis Root Cells. *Bio Protoc* **7**, e2240 (2017).

10 Zhang, H. *et al.* Large-scale identification of potential phase separation proteins from plants using a cell-free system. *Mol Plant* **16**, 310–313 (2023).

11 Fang, X., Cui, Y., Li, Y. & Qi, Y. Transcription and processing of primary microRNAs are coupled by Elongator complex in Arabidopsis. *Nat Plants* **1**, 15075 (2015).

12 Missra, A. & von Arnim, A. G. in *Plant Circadian Networks: Methods and Protocols* (ed Dorothee Staiger) 157–174 (Springer New York, 2014).

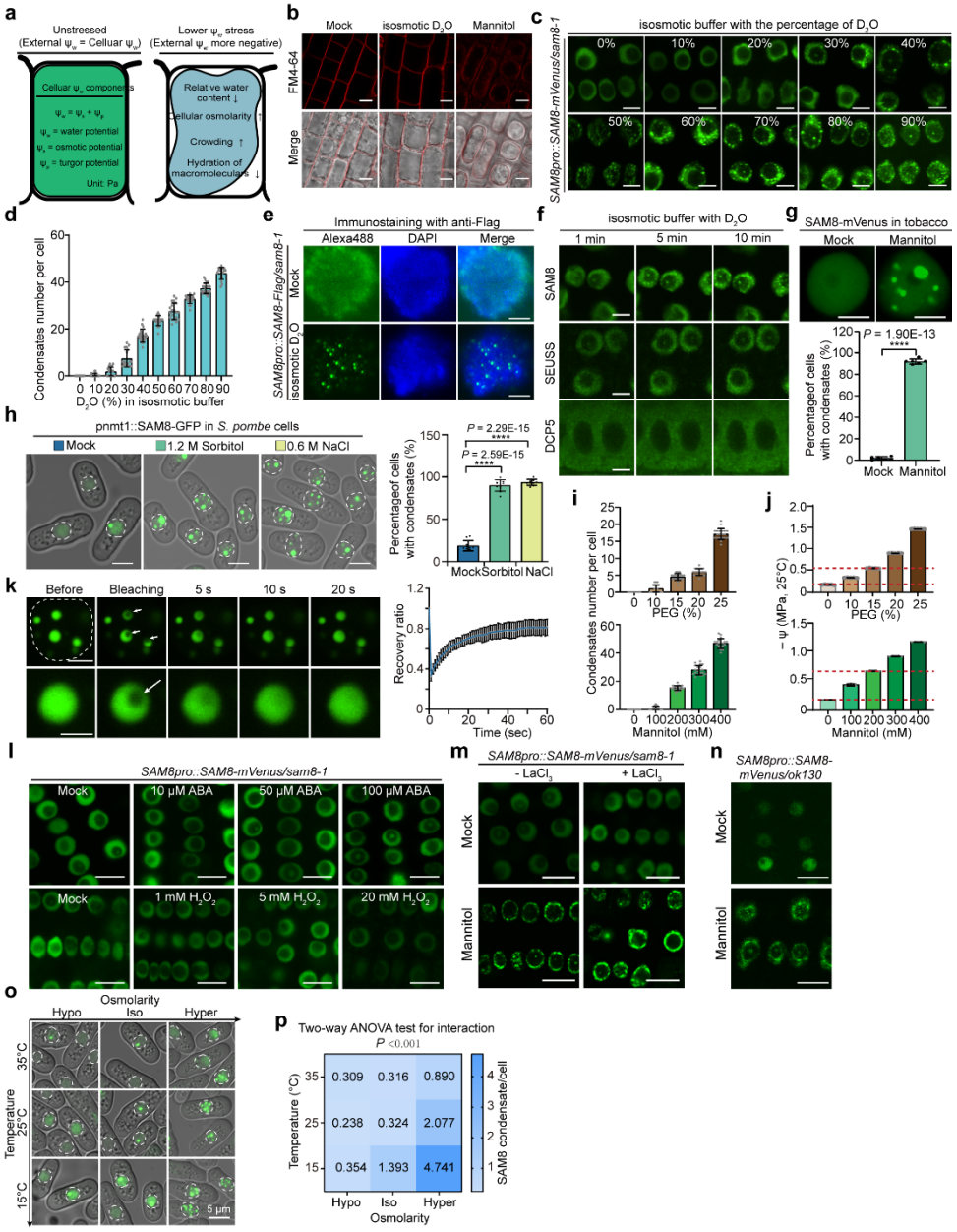

Extended Data Fig. 1 | SAM8 condensation in cells is dependent on water potential reduction.

a, Schematic representation of a plant cell under unstressed conditions (left) and under lower water potential stress (right). Under normal conditions, cellular water potential (φ_w) is balanced with the external environment and is defined by the sum of osmotic potential (φ_s) and turgor pressure (φ_p). When external water potential becomes more negative (hyperosmotic stress), cellular water loss results in reduced relative water content, increased cellular osmolarity, enhanced macromolecular crowding, and diminished hydration of intracellular macromolecules. **b**, Confocal microscopy of Arabidopsis root tip cells that are treated with 95% D_2O or 800 mM Mannitol for 10 min. FM4-64 was used to label the plasma membrane. **c**, Representative confocal images of Arabidopsis root tip cells expressing SAM8-GFP. The cells were treated with the indicated D_2O concentration for 5 min. **d**, Quantification of the number of condensates per cell

shown in (b). (n = 20). **e**, Immunostaining of root tip nuclei from Arabidopsis expressing SAM8-Flag. The roots were treated with an isosmotic buffer prepared with H_2O or D_2O. **f**, Representative confocal images of Arabidopsis root tip cells expressing SEUSS-GFP, and DCP5-GFP. The cells were treated with an isosmotic buffer prepared with D_2O. **g**, Top, representative confocal images showing SAM8 condensation in tobacco epidermal cell nuclei upon 300 mM mannitol treatment for 30 min. Bottom, the percentage of cells containing condensates. (n = 6). **h**, Left, representative confocal images of *Schizosaccharomyces pombe* cells expressing SAM8-GFP. The cells were treated with indicated concentration of sorbitol or NaCl for 10 min. Right**,** the percentage of cells containing SAM8 condensates shown in left. (n = 10 replicates, with each replicate containing approximately 200 cells). Asterisks indicate significant differences (two-tailed *t* test). **i**, Quantification of the condensate number per cell in Arabidopsis root tip cells expressing SAM8. The cells were treated with indicated concentration of PEG or mannitol for 10 min. (n = 20). **j**, Vapour-pressure osmometry measurement of the water potential for the indicated concentrations of PEG8000 and D-Mannitol at 25°C. (n = 5). **k,** Left, FRAP of SAM8 condensates in tobacco epidermal cells. The dashed line delineates the border of a nucleus. White arrows indicate the bleached area. Right**,** plot showing the fluorescence recovery of SAM8 condensates after photobleaching. (n = 15). **l, m,** Representative confocal images of Arabidopsis root tip cells expressing SAM8-mVenus. The cells were treated as indicated. **n**, Representative confocal images of Arabidopsis root tip cells from *ok130* mutant expressing SAM8. The cells were treated as indicated. **o**, Representative confocal images of *Schizosaccharomyces pombe* cells expressing SAM8-GFP. The cells were treated as indicated. **p,** Two-way ANOVA statistical analysis showing the interaction between temperature and osmolarity on SAM8 condensation in yeast cells. At least 155 cells were analyzed for each condition. For (c and f-j), Error bars indicate mean ± SD. Scale bars, 10 μm (a, h and k-m), 5 μm (b, e-g and n), 2 μm (d).

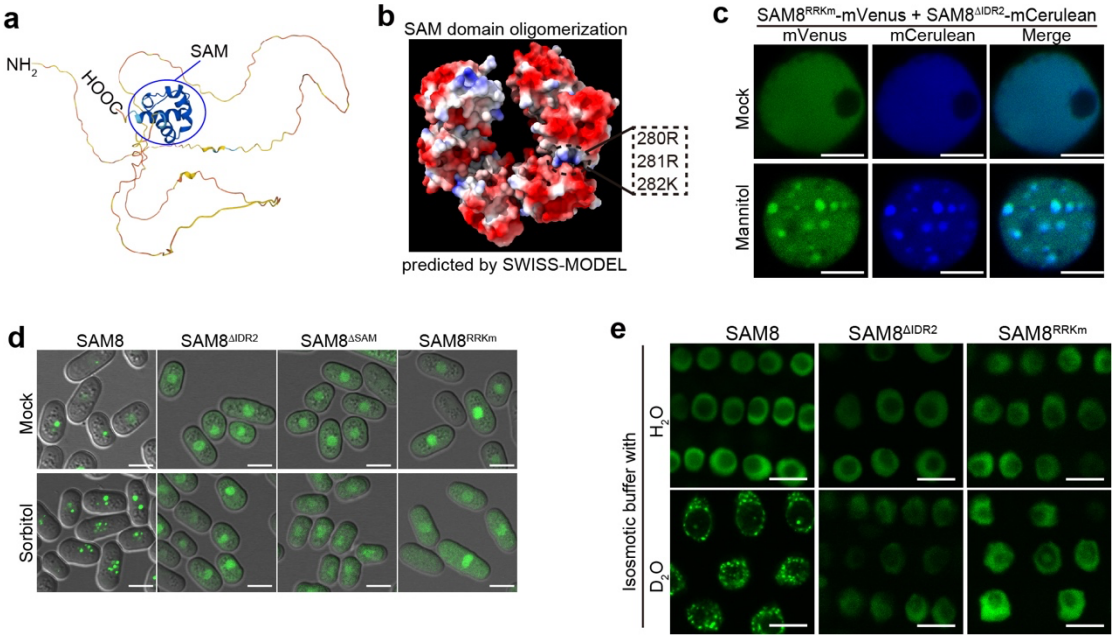

Extended Data Fig. 2 | IDR2 and the SAM domain are both necessary for SAM8 condensation.

a, The structure of SAM8 as predicted by AlphaFold. The blue circle indicates the SAM domain. **b,** The oligomerization of SAM domain as predicted by SWISS-MODEL. The dotted circle indicates three key amino acids at the oligomerization interface. **c,** Representative confocal images of tobacco epidermal cells co-expressing SAM8^{RRKm} and SAM8$^{\Delta IDR2}$. The cells were treated with or without 0.3 M mannitol. Scale bar, 5 μm. **d,** Representative confocal images of *Schizosaccharomyces pombe* cells expressing SAM8-GFP or its variants. The cells were treated with or without 1.2 M sorbitol. Scale bars, 5 μm. **e**, Representative confocal images of Arabidopsis root tip cells expressing SAM8 and variants treated with an isosmotic buffer prepared with H_2O or 90% D_2O for 10 min. Scale bars, 10 μm.

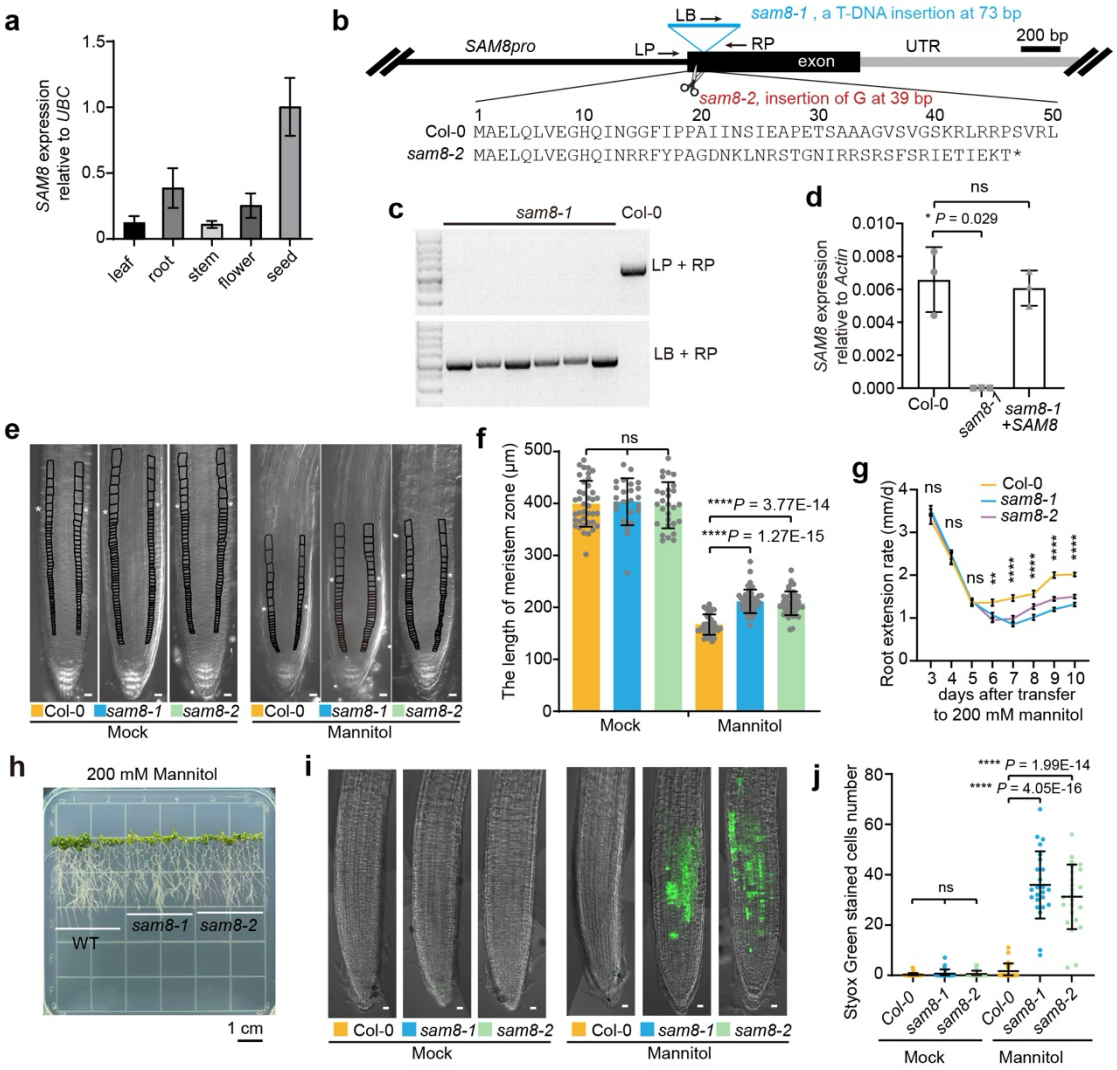

Extended Data Fig. 3 | SAM8 is required for stress tolerance under osmotic conditions.

a, The expression of *SAM8* relative to *UBC* in different tissues as determined by quantitative RT-PCR. Error bars indicate mean ± SD (n = 3). **b**, Illustration of the *SAM8* genomic locus. The thick black box indicates the exon, the thin grey box indicates the UTR, and the black line indicates the promoter. The information of *sam8-1* and *sam8-2* is indicated in blue and red, respectively. The translation product of the *sam8-2* mRNA is shown at the bottom. **c,** Electrophoresis of PCR amplification products using primers indicated in (b). For gel source data, see Supplementary Figure 1. **d,** The relative expression of *SAM8* to *ACTIN* in indicated genotypes as determined by quantitative RT-PCR. Error bars indicate mean ± SD (n = 3). **e**, Confocal images of longitudinal root tips from 7-day-old seedlings grown vertically on mock or mannitol medium for 2 days. The white asterisks indicate the meristematic cortex. Scale bars, 20 μm. **f,** Quantification of the length of the meristem zone shown in (e). Error bars indicate mean ± SD (n = 24-46). Asterisks indicate significant differences (two-tailed *t* test). **g**, Quantification of the root extension rate of Arabidopsis seedlings that were transferred to medium supplemented with 200 mM mannitol.

Error bars indicate mean ± SE (n = 30). Asterisks indicate significant differences (two-tailed *t* test). ns, not significant. **h**, Representative images of Arabidopsis seedlings that grew for 10 days upon transferring to medium supplemented with 200 mM mannitol. Scale bars, 1 cm. **i**, Cell death staining of *Arabidopsis* roots using SYTOX green upon 300 mM mannitol treatment for 2 h. Scale bars, 20 μm. **j**, The SYTOX green-stained cell numbers shown in (i). Error bars indicate mean ± SD (n = 24 roots). Asterisks indicate significant differences (two-tailed *t* test), ns, not significant.

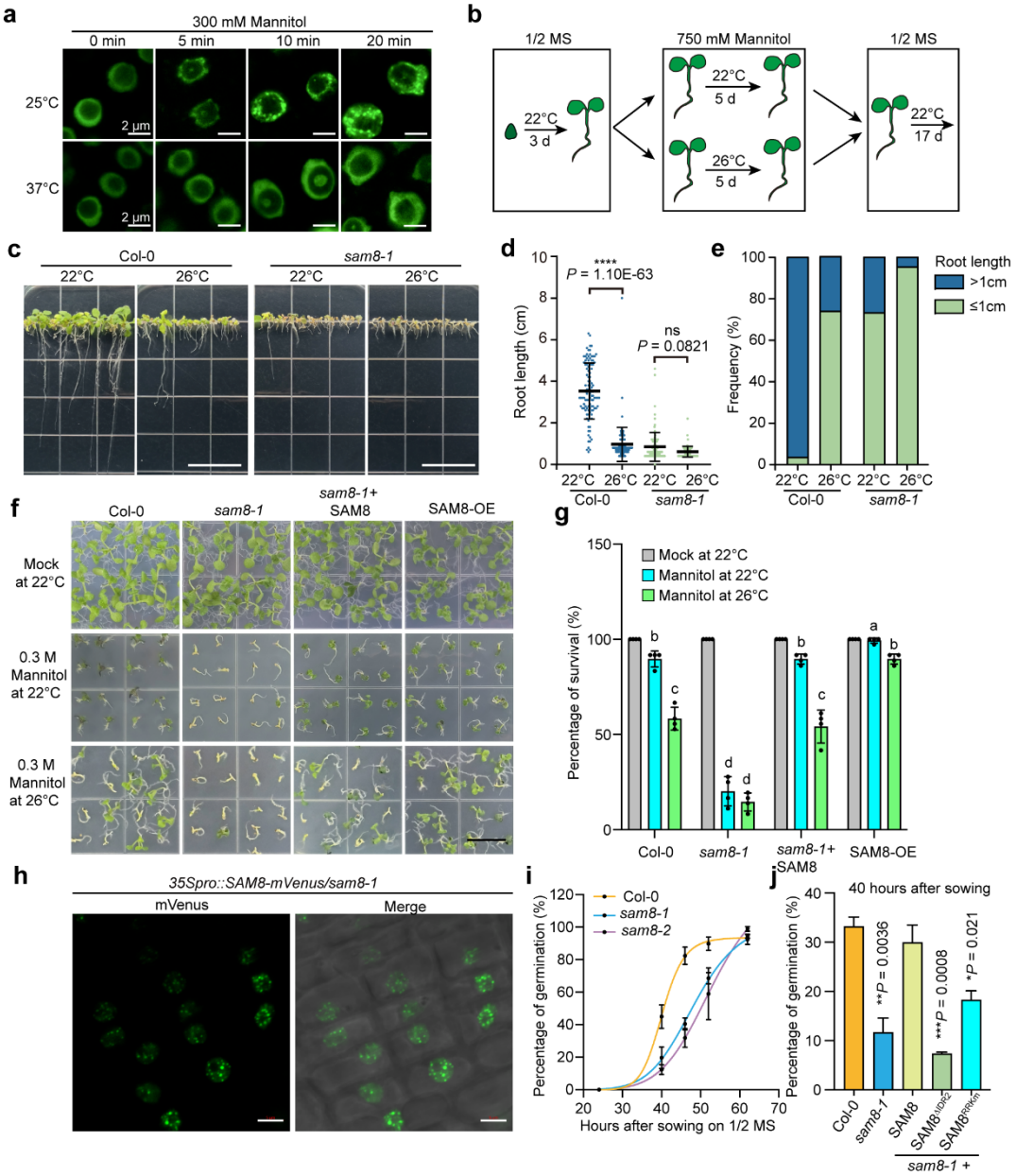

Extended Data Fig. 4 | SAM8 condensation is crucial for osmotic stress tolerance.

a, Confocal imaging of Arabidopsis root tip cells expressing SAM8-mVenus with indicated treatment. Scale bars, 2 μm. **b,** The procedure of the seedling transfer assay. **c,** Representative images of indicated genotypes tested in the transfer assay shown in (b). Scale bars, 2 cm. **d,** Quantification of the root length of seedlings shown in (c). Error bars indicate mean ± SD. Asterisks indicate significant differences (two-tailed *t* test), ns, not significant. **e,** The frequency of seedlings with root length bigger or smaller than 1 cm for the seedlings shown in (c). **f,** Representative images of 12-day-old seedlings of indicated genotypes grown under conditions as indicated. Scale bar, 1 cm. **g,** Quantification of survival percentage shown in (f). Error bars indicate mean ± SD (n = 4 replicates with each replicate containing approximately 24 plants). Different letters indicate statistically significant differences between samples (one-way ANOVA

followed by the least significant difference test). **h,** Representative confocal images of Arabidopsis root tip cells overexpressing SAM8. Scale bars, 5 μm. **i, j,** Quantification of germination percentage of indicated genotypes. Error bars indicate mean ± SD (n = 3 with each replicate containing approximately 300 seeds).

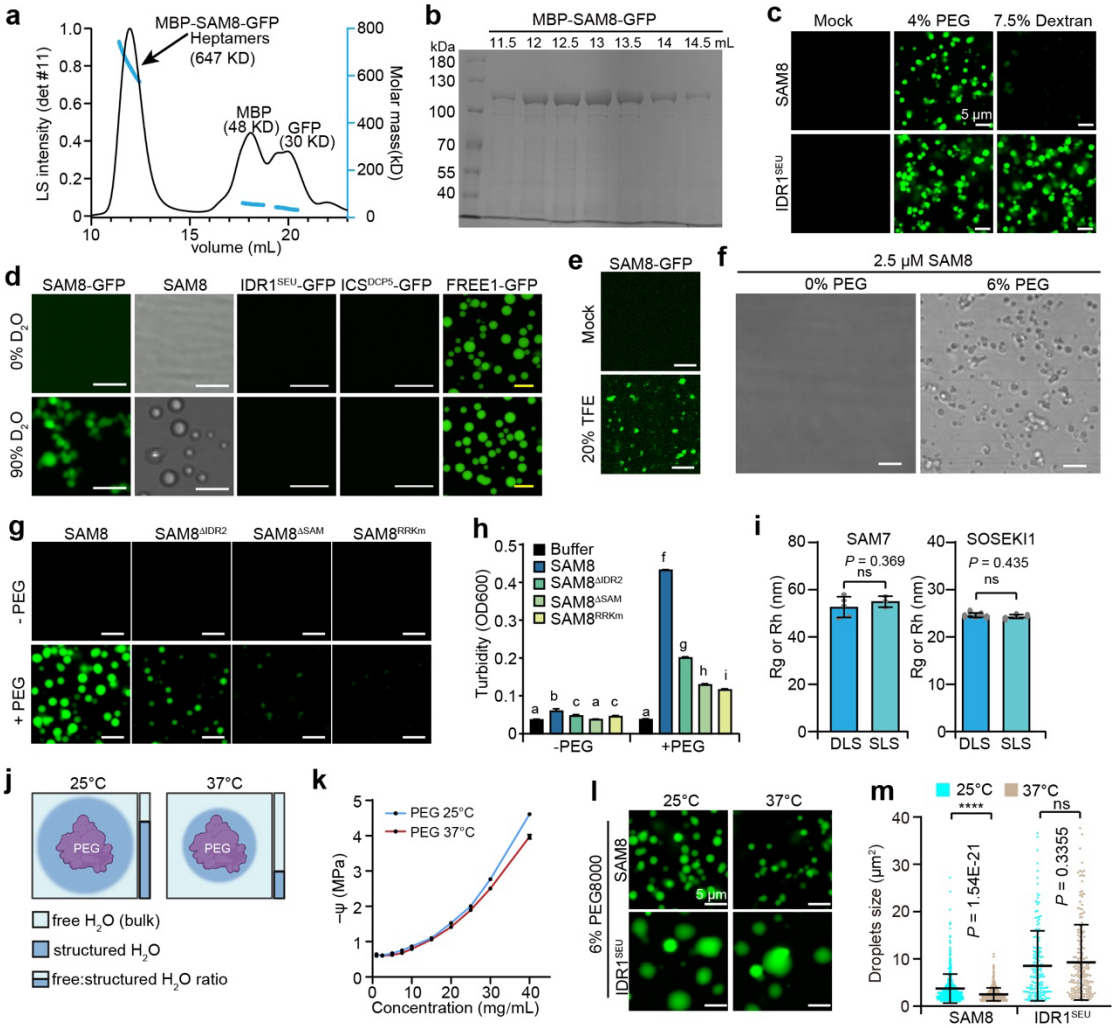

Extended Data Fig. 5 | SAM8 condensation in vitro is sensitive to water potential change.

a, SEC-MALS assay showing the size of MBP-SAM8-GFP. Left y-axis, the light scattering intensity from the 90° detector (detector 11). Right y-axis, molecular weight. **b**, SDS-PAGE and Coomassie blue staining of samples from gel-filtration assay. For gel source data, see Supplementary Figure 1. **c**, In vitro phase separation assay of 2.5 μM SAM8-GFP and IDR1^{SEU} under the indicated conditions. Scale bars, 5 μm. **d,** In vitro phase separation assay of 10 μM SAM8-GFP, SAM8-His, SEU^{IDR1}-GFP, DCP5^{ICS}-GFP and FREE1-GFP in the presence of 90% D_2O. Scale bars: white, 2 μm; yellow, 10 μm. **e,** In vitro phase separation assay of 2.5 μM SAM8-GFP proteins in the presence of TFE. Scale bars, 5 μm. **f,** In vitro phase separation assay of 2.5 μM unlabeled SAM8 with or without PEG. Scale bars, 5 μm. **g,** In vitro phase separation assay of 2.5 μM SAM8-GFP and its variants with or without 6% PEG 8000. Scale bars, 5 μm. **h,** Turbidity measurement of 2.5 μM SAM8-GFP and its variants with or without 6% PEG 8000. Error bars indicate mean ± SD (n = 10). Different letters indicate statistically significant differences between samples (one-way ANOVA followed by the least significant difference test, $P < 0.05$). **i**, Measurement of Rg and Rh for SAM7, and SOSEKI1 by DLS and SEC-MALS (SLS), respectively. Error

bars indicate mean ± SD (n = 5 for DLS, n = 3 for SLS). Asterisks indicate significant differences (two-tailed *t* test). ns, not significant. **j,** Schematic illustration showing the effect of PEG on free/structured water ratio at two temperatures. **k,** Vapour-pressure osmometry measurement of the water potential for different concentrations of PEG8000 solution at indicated temperatures. Error bars indicate mean ± SD (n = 5). **l,** In vitro phase separation assay of 2.5 μM SAM8-GFP and IDR1^{SEU} under indicated conditions. Scale bars, 5 μm. **m,** Quantification of the average droplet size shown in (e). Error bars indicate mean ± SD. Asterisks indicate significant differences (two-tailed t test). ns, not significant.

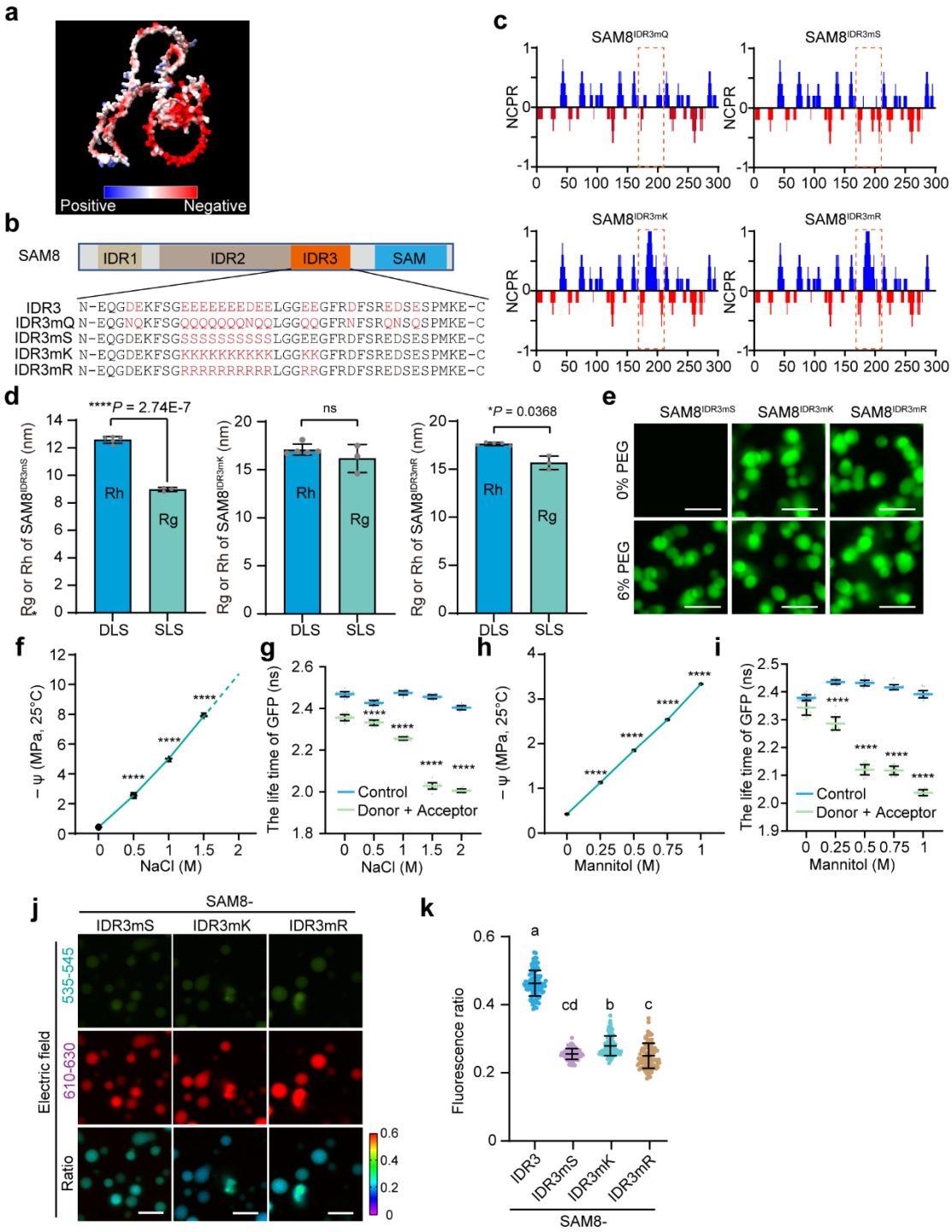

Extended Data Fig. 6 | The role of IDR3 in SAM8 condensation.

a, The electrostatic surface analysis of SAM8 protein. Blue color indicates net positive charges and red color indicates net negative charges. The structure of SAM8 was predicted by AlphaFold Server and visualized by ChimeraX. **b**, The amino acid sequence of IDR3 or IDR3 variants. **c**, The net charge per residue of SAM8 variants as predicted by CIDER webserver. **d**, Measurement of Rg and Rh for SAM8 variants by DLS and SEC-MALS (SLS), respectively. Error bars indicate mean ± SD (n = 5 for DLS, n = 3 for SLS). Asterisks indicate significant differences (two-tailed *t* test). ns, not significant. **e**, In vitro phase

separation assay of 2.5 μM SAM8 variants in the presence of PEG8000. Scale bars, 5 μm. **e**, **g**, Vapour-pressure osmometry measurement of the water potential for indicated concentrations of NaCl, or D-Mannitol. Error bars indicate mean ± SD (n = 5). **f**, **h**, The lifetime of donor GFP for the indicated proteins in the presence of the indicated concentrations of agents. Error bars indicate mean ± SD (n = 20). **i**, Confocal imaging of 5 μM SAM8 and SAM8^{IDR3m} in the presence of DI-4-ANEPPS dye. Scale bars, 10 μm. **j**, The ratio of emission at 535–545 and 610–640 nm shown in (i). Error bars indicate mean ± SD (n = 98). Different letters indicate statistically significant differences between samples (one-way ANOVA followed by the least significant difference test, $P < 0.05$). For (e-h), Statistical significance details are provided as Source Data.

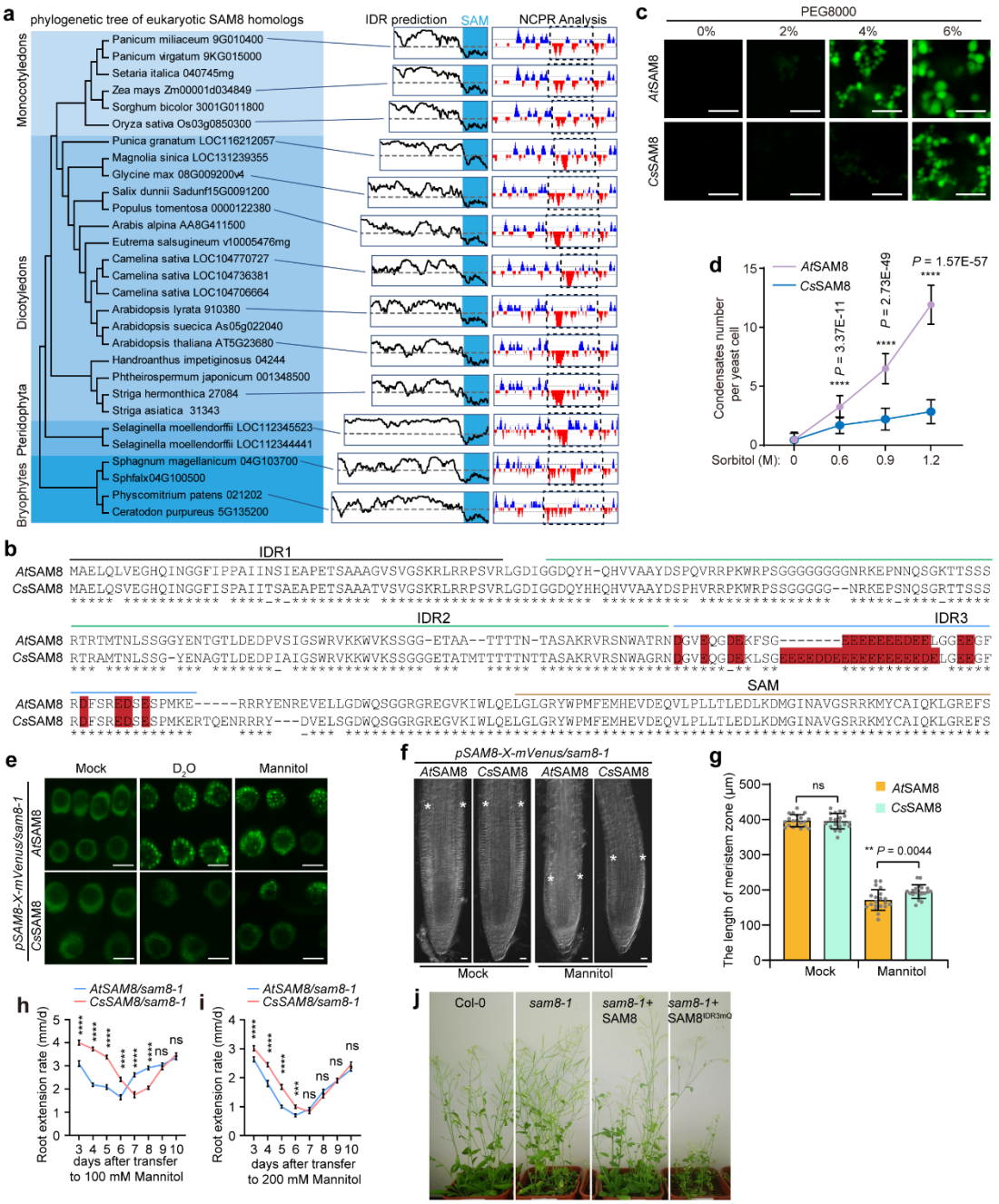

Extended Data Fig. 7 | Conservation analysis of SAM8.

a, Left, neighbor-joining phylogenetic tree of SAM8 homologs. Middle, IDR predictions of SAM8 homologs. Blue boxes indicate SAM domain. Right, NCPR analyses of SAM8 homologs. Blue color indicates net positive charges and red color indicates net negative charges. The dashed boxes indicate negatively charged IDR3 region. **b,** Alignment of SAM8 sequences from *Arabidopsis thaliana* (*At*) and *Camelina sativa* (*Cs*). The negatively charged residues in IDR3 are indicated in red. **c**, In vitro phase separation assay of 2.5 μM *At*SAM8-GFP and *Cs*SAM8-GFP in the presence of indicated concentrations of PEG8000. Scale bars, 5 μm. **d**, The condensate number per cell when yeast cells expressing *At*SAM8-GFP and *Cs*SAM8-GFP were treated with the indicated concentrations of sorbitol. Error bars indicate mean ± SD (n = 60).

Asterisks indicate significant differences (two-tailed *t* test). **e**, Confocal microscopy of Arabidopsis root tip cells expressing *At*SAM8-GFP or *Cs*SAM8-GFP. The cells were treated with isosmotic 90% D_2O buffer or 0.3 M mannitol. Scale bars, 5 μm. **f**, Confocal images of longitudinal root tips from 7-day-old seedlings grown vertically on mock or mannitol medium for 2 days. The white asterisks indicate the meristematic cortex. Scale bars, 20 μm. **g**, Quantification of the length of meristem zone shown in (f). Error bars indicate mean ± SD (n = 20). Asterisks indicate significant differences (two-tailed *t* test), ns, not significant. **h, i,** Quantification of the root extension rate of Arabidopsis seedlings that were transferred to medium supplemented with 100 or 200 mM mannitol. Error bars indicate mean ± SE (n = 30). Asterisks indicate significant differences (two-tailed *t* test). ns, not significant. **j**, Representative images of adult plants of indicated genotypes under normal conditions.

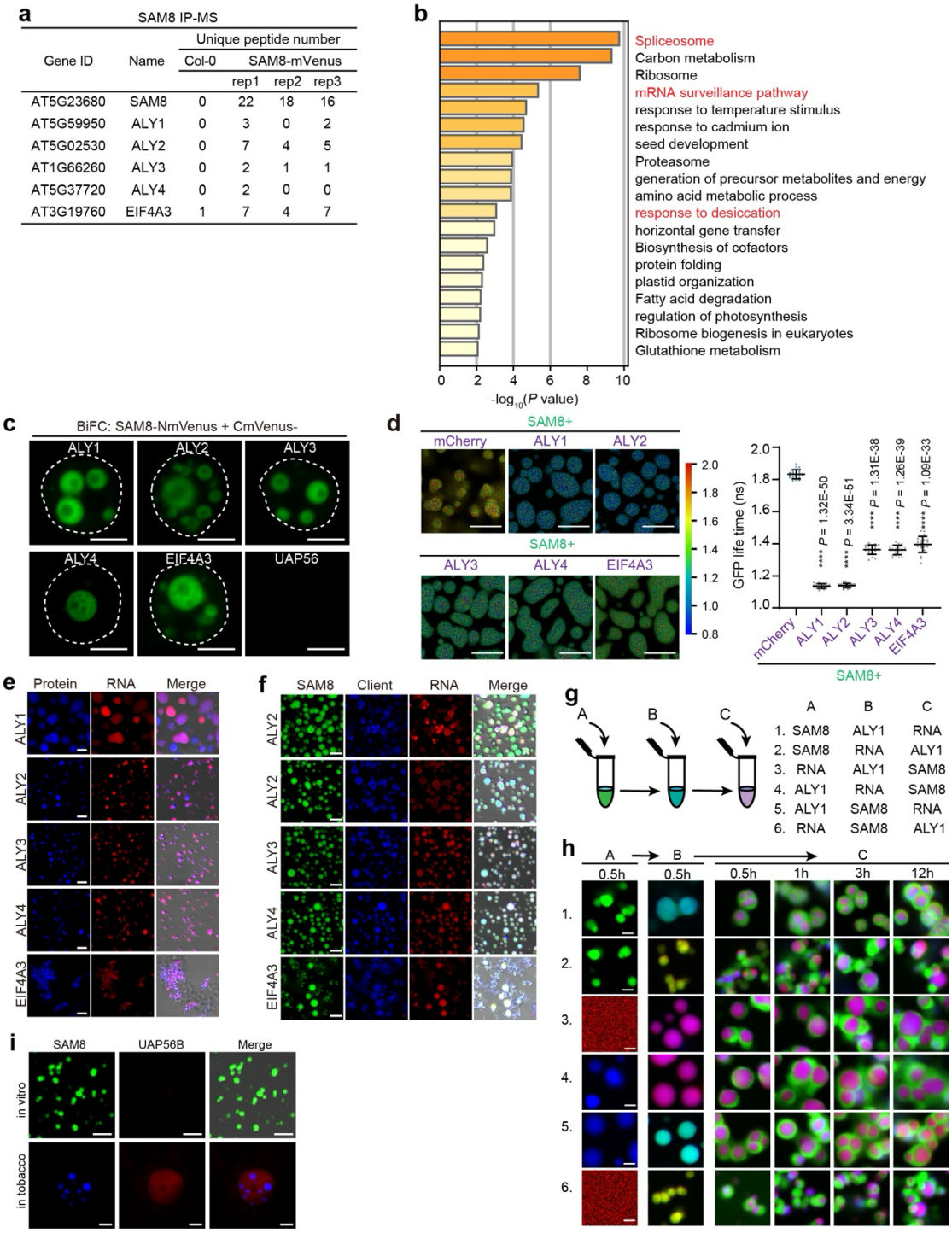

Extended Data Fig. 8 | SAM8 condensates selectively partition RNA export factors.

a, SAM8 interacting proteins enriched by IP-MS from 10-days-old Arabidopsis seedlings expressing SAM8-mVenus upon 300 mM mannitol treatment for 1 h. **b**, Gene Ontology analysis of the enriched proteins by SAM8-IP-MS. **c,** BiFC analysis of the interactions between SAM8 and ALYs, EIF4A3 and UAP56B upon co-expression in tobacco epidermal cells. Scale bars, 5 μm. Dashed circles indicate the borders of nuclei. **d**, Left, FLIM-FRET images of 5 μM SAM8 droplets incubated with mCherry-ALYs. Scale bars, 10 μm. Right, the lifetime

of donor GFP for the combinations shown on the left. Error bars indicate mean ± SD (n = 22). Asterisks indicate significant differences (two-tailed *t* test). **e,** In vitro phase separation assay of 2.5 μM ALYs-BFP or EIF4A3-BFP in the presence of Cy5-labelled RNA. Scale bars, 10 μm. **f,** In vitro phase separation assay of 2.5 μM SAM8-GFP in the presence of both ALYs-BFP or EIF4A3-BFP and Cy5-labelled RNA. Scale bars, 10 μm. **g**, Illustration of different orders of component addition for sub-phase formation within SAM8 droplets. **h**, Time-lapse imaging of sub-phase formation within SAM8 droplets. Scale bars, 2 μm. **i,** Top, in vitro phase separation assay of 2.5 μM SAM8-GFP in the presence of UAP56B-BFP. Bottom, representative confocal images of tobacco epidermal cells co-expressing SAM8-mVenus and UAP56B-mCherry. Scale bars, 5 μm.

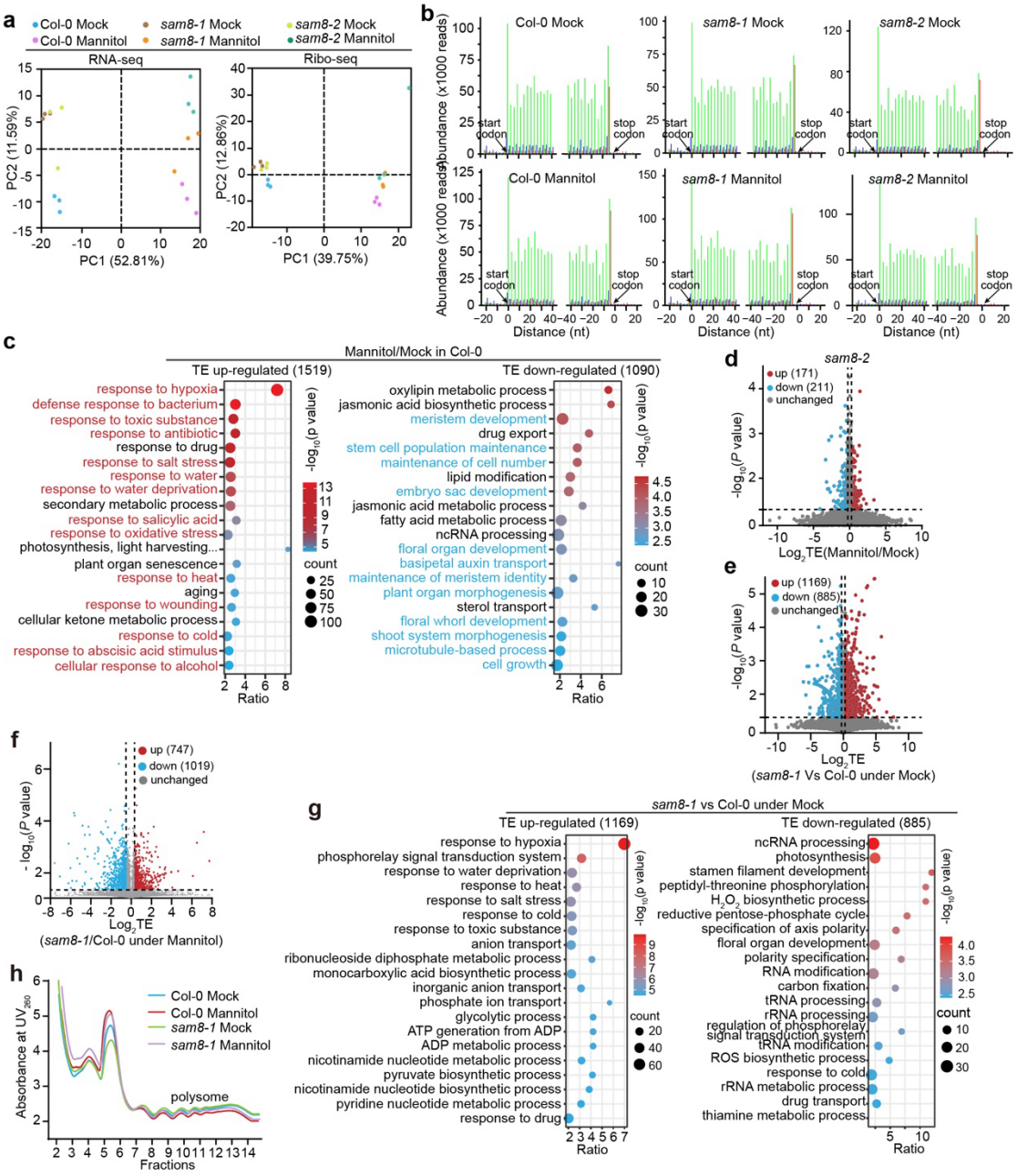

Extended Data Fig. 9 | SAM8 functions in translation reprogramming upon osmotic stress.

a, Principal component analysis (PCA) of the RNA-seq and Ribo-seq data as indicated. **b**, The 3-nt periodicity analysis of the Ribo-seq reads mapped between the start codon and stop codon. **c**, Top 20 enriched GO terms for TE up- and down-regulated genes in Col-0 upon mannitol treatment versus mock. Stress- and development-related items are highlighted in red and blue, respectively. **d**, Volcano plot showing the translation efficiency (TE) change under mannitol treatment compared to mock in *sam8-2*. **e**, **f**, Volcano plot showing the TE change in *sam8-1* versus Col-0 under normal conditions (e) and osmotic treatment (f). **g**, Top 20 enriched GO terms for TE up- and down-regulated genes in *sam8-1* versus Col-0 under normal conditions. **h**, Polysome

profiling of 5-day-old Col-0 and *sam8-1* seedlings with or without 0.3 M mannitol treatment for 1 hour.

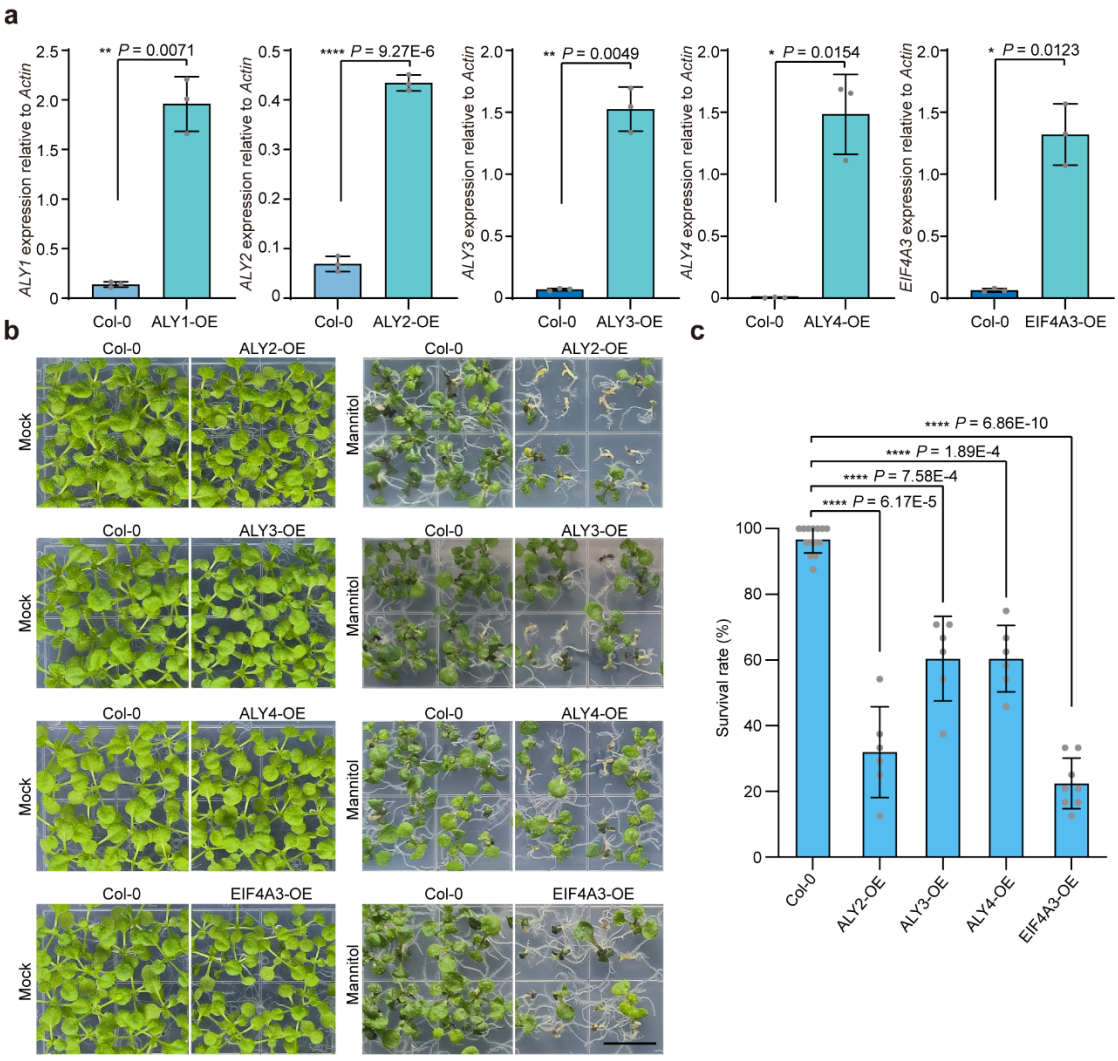

Extended Data Fig. 10 | Overexpression of ALYs or EIF4A3 results in hypersensitivity to osmotic stress.

a, The relative expression of *ALY1-4* and *EIF4A3* to *ACTIN* in indicated genotypes as determined by quantitative RT-PCR. Error bars indicate mean ± SD (n = 3). **b,** Representative image of 12-day-old seedlings of indicated genotypes grown on medium with or without 300 mM mannitol. OE, overexpression. Scale bars, 1 cm. **c,** Quantification of survival rate of genotypes shown in (b). Error bars indicate mean ± SD (n = 6 replicates with each replicate containing approximately 24 plants). Asterisks indicate significant differences (two-tailed *t* test).